

# A Sharp Free Surface Finite Volume Method Applied to Gravity Wave Flows

Vuko Vukčević<sup>a</sup>, Johan Roenby<sup>b</sup>, Inno Gatin<sup>a</sup>, Hrvoje Jasak<sup>a,c,\*</sup>

<sup>a</sup>University of Zagreb, Faculty of Mechanical Engineering and Naval Architecture, Ivana Lučića 5, Zagreb, Croatia

<sup>b</sup>Stromning, Luftmarinegade 62, DK-1432, Copenhagen K, Denmark

<sup>c</sup>Wikki Ltd, 459 Southbank House, SE1 7SJ, London, United Kingdom

---

## Abstract

This paper presents a sharp free surface method for fully nonlinear flow of two immiscible phases for wave propagation problems in the Finite Volume framework. The method resolves a sharp interface between two phases by combining the geometric reconstruction Volume-of-Fluid scheme `isoAdvector` for accurate advection of the free surface with the Ghost Fluid Method for the consistent treatment of density and pressure gradient discontinuities at the free surface. The method uses a compact computational stencil irrespective of cell shape and is formally second-order accurate in time and space. The primary focus of this work is to present the combined method and verify and validate it for wave-related problems in ocean sciences, marine and coastal engineering, by considering the following test cases: i) wave propagation of a two-dimensional wave with moderate steepness, ii) green water (water-on-deck) simulations for a ship model with violent free surface flow patterns. The method is implemented in OpenFOAM, an open source software for Computational Fluid Dynamics.

*Keywords:*

Free surface flow, Geometric reconstruction Volume-of-Fluid method `isoAdvector`, Ghost Fluid Method, OpenFOAM, Wave propagation and loads, Verification and validation

---

## 1. Introduction

Computational Fluid Dynamics (CFD) tools for free surface flows are becoming increasingly popular due to increased availability of computational resources required for this type of simulations in both scientific and industrial setting. Two-phase CFD simulations represent an important addition to Experimental Fluid Dynamics (EFD), where highly resolved Direct Numerical Simulations (DNS) [1] provide detailed information of flow features, which may be used to investigate underlying physical mechanisms in free surface flows with complex topological changes (*e.g.*

---

\*Corresponding author.

*Email addresses:* vuko.vukcevic@fsb.hr (Vuko Vukčević), johan.roenby@gmail.com (Johan Roenby), inno.gatin@fsb.hr (Inno Gatin), hrvoje.jasak@fsb.hr (Hrvoje Jasak), h.jasak@wikki.co.uk (Hrvoje Jasak)

plunging breaking wave [2]). The CFD methods for free surface flows have a wide range of applications for industrially relevant problems, such as marine hydrodynamics [3, 4], wave propagation and load assessment [5, 6], seakeeping of offshore platforms and ships [7, 8], *etc.*

The presence of a free surface implies a discontinuity in pressure and velocity gradient tangential to the interface [9]. In recent years, substantial research effort has been undertaken in order to numerically handle the discontinuities, where a number of different methods has emerged, most of them relying on the Eulerian approach. One of the first methods adopted by many authors is based on diffusive interface modelling and conditional averaging [10], where two sets of governing equations for two fluids are combined in a single set of equations with density and viscosity varying across the interface based on the volume fraction [11]. Similar methods are still popular for simulations of gravity waves [12, 13, 14, 15], where the numerical smearing of the interface dictates the resolution of pressure discontinuities. In sharp interface methods, two similar approaches are used to treat the discontinuities at the free surface: the Ghost Fluid Method (GFM) [16, 17] and the Embedded Free Surface (EFS) method [18]. Both methods assume a single-fluid formulation with special interpolation schemes handling the discontinuities, while their difference lies in the numerical discretisation of interface jump conditions [18]. The GFM has been first introduced by Fedkiw *et al.* [16] in a finite difference framework. The GFM has been used alongside the Level Set (LS) interface capturing method to ensure sharp interface reconstruction, where layers of ghost cells (nodes) have been used to extrapolate the fields from one-side of the interface. The GFM has been extended to free surface incompressible flows with large density variations [19], where it is also used alongside a variant of LS method that ensures mass conservation [20]. More recent works include the extension of the method to compressible two-phase flows by Bo and Grove [21] using the Volume-of-Fluid (VOF) method and an extensive review of different treatments of tangential stress balance at the interface in two-phase incompressible flow by Lalanne *et al.* [22]. Most of the publications use either finite differences or finite volumes for spatial discretisation on structured grids. Queutey and Visonneau [23] present a method for handling free surface discontinuities in arbitrary polyhedral Finite Volume (FV) framework, where the interface is assumed to be aligned with the grid faces. Such a procedure imposes restrictions in terms of grid refinement near the free surface. The method resembles the GFM as used by other authors in the same field (*e.g.* Huang *et al.* [24]), although no comments have been made on their similarities and differences. The GFM has been recently extended to arbitrary polyhedral FV framework by Vukčević *et al.* [25], where no a-priori assumptions have been made on the location of the interface. Although the method ensures consistent treatment of discontinuities across the interface even with the algebraic VOF method for interface capturing [11, 26], the numerical diffusion of the volume fraction field cannot be easily controlled.

In order to avoid the problem of controlling the numerical diffusion of the volume fraction field in case of com-

plex flow patterns, a better alternative to interface advection scheme needs to be considered. The two most established methods for interface advection in Eulerian framework found in the literature [27] are: geometrically reconstructed Volume-of-Fluid (VOF) method [28, 29] and the Level Set (LS) method [30, 31, 32]. In LS, a colour function based on signed distance profile [31] is used, where the zero level set represents the sharp interface. Without a special treatment, the LS method is not conservative [19, 32] and the colour function often loses the signed distance property during the numerical advection step due to discretisation errors. The latter problem is by various redistancing algorithms. The most direct approach is the actual calculation of the smallest distance to the zero level set surface [33]. Costly direct calculation can be avoided if one solves an Eikonal equation which forces the gradient of the colour function to be equal to unity [34]. Both strategies are often performed only in a narrow band near the interface in order to minimise the computational effort. Sun and Beckermann [35, 36] presented an alternative LS advection equation derived from diffusive interface Phase Field equation. The resulting transport equation has additional terms that serve to keep the signed distance profile of a colour function during the advection step. The method has been recently extended to unstructured polyhedral FV grids [37], where the authors have shown that all the additional terms can be treated in an implicit manner. Such a procedure works well for wave propagation problems since the diffusion of the interface is a user-defined parameter and the signed distance field is well preserved [38], although there is no guarantee that phase mass conservation will be preserved.

Geometric VOF methods rely on the volume fraction field in order to reconstruct and advect the interface. These methods have proven to be very accurate and efficient [28, 39, 40] on structured, hexahedral grids. Substantial research has also been devoted to interface reconstruction on unstructured grids [41, 42]. Although the methods have proved to be accurate even on unstructured grids, their performance is significantly limited by complicated geometric operations they require. Recently, Roenby *et al.* [29] presented the `isoAdvect` algorithm developed in OpenFOAM [43] which is computationally efficient since it keeps costly geometric operations to a minimum. The geometric reconstruction step uses the volume fraction field interpolated from cell-centres to all points of arbitrary polyhedral cells, while the advection step is based on analytically evaluating the flux of one fluid through a polygonal face within a time-step.

The aim of this work is to combine the `isoAdvect` method [29] and the Ghost Fluid Method [25] and apply it to accurate simulations of gravity wave related two-phase flows. In recent years, CFD tools have been extensively used for wave propagation problems [12, 13, 44, 5, 14, 6, 15], with a focus on establishing accuracy and maturity of the applied toolboxes. Although some of the authors indeed perform grid sensitivity studies, they do not report achieved orders of accuracy and the corresponding numerical uncertainty following the guidelines in the established literature [45, 46]. In this work, we follow the least squares procedure by Eça and Hoekstra [47] to assess the numer-

ical uncertainty and achieved order of accuracy of the proposed, formally second order accurate approach.

The paper is organised as follows. First, the mathematical model of incompressible, free surface flow in a single-fluid formulation is presented. Second, the numerical details of the Ghost Fluid Method are presented, followed by the formulation of the `isoAdvector` method for interface advection. Third, a set of relevant verification and validation test cases is presented. Verification is first performed on a wave propagation case, where the achieved order of accuracy and numerical uncertainty are assessed in detail. The estimates on dissipation and dispersion errors during wave propagation in a long numerical wave tank are also provided. Additional test case presents verification and validation study for a violent free surface flow occurring on a deck of a simplified ship model in regular waves, comparing the results to experimental data by Lee *et al.* [48].

## 2. Mathematical Model

We consider two incompressible, Newtonian fluids separated by a sharp interface in a gravitational field. The motion of each fluid is governed by Navier–Stokes equations in primitive form together with the incompressibility constraint [20]:

$$\frac{\partial \mathbf{u}}{\partial t} + \nabla \cdot (\mathbf{u}\mathbf{u}) - \nabla \cdot (\nu \nabla \mathbf{u}) = -\frac{1}{\rho} \nabla p_d, \quad (1)$$

$$\nabla \cdot \mathbf{u} = 0. \quad (2)$$

Here  $\mathbf{u}$  is the velocity field, and  $\nu$  is the kinematic viscosity field assumed to take different constant values,  $\nu^+$  and  $\nu^-$ , in each of the two fluids. Similarly,  $\rho$  is the density field taking different constant values,  $\rho^+$  and  $\rho^-$ , in each fluid. The quantity  $p_d$  in Eqn. (1) is the dynamic pressure defined as the pressure field,  $p$ , with the hydrostatic potential subtracted:

$$p_d = p - \rho \mathbf{g} \cdot \mathbf{x}, \quad (3)$$

where  $\mathbf{g}$  is the gravitational acceleration and  $\mathbf{x}$  is the position vector. For two-fluid problems we must also account for the position and motion of the fluid interface, on which appropriate boundary conditions must be imposed. In what follows, we will work with a slightly simplified form of jump conditions at the interface, neglecting surface tension effects and the effect of tangential stress balance compared to normal stress balance [49]. This assumption is justified for flows with large Weber and Reynolds numbers that are of interest in this work, as discussed by Huang *et al.* [24] in detail. The jump conditions are briefly outlined here, while the reader is referred to [49] for a detailed analysis.

- Density discontinuity:

$$[\rho] = \rho^- - \rho^+, \quad (4)$$

where  $[\cdot]$  notation is taken from the GFM literature [20, 24] and denotes the jump in variables across the free surface. Superscripts  $^+$  and  $^-$  denote the values infinitesimally close to the free surface in heavier and in lighter fluid, respectively.

- Kinematic boundary condition:

$$[\mathbf{u}] = \mathbf{u}^- - \mathbf{u}^+ = \mathbf{0}. \quad (5)$$

Kinematic boundary condition ensures the continuity of the velocity field at the free surface.

- Simplified tangential stress balance:

$$[\nabla_n \mathbf{u}_t] = \mathbf{0}, \quad (6)$$

stating that the normal gradient of the tangential velocity field does not have a jump. This simplified form is obtained by neglecting surface divergence of surface tension force and surface gradient of the normal velocity component [49].

- Dynamic boundary condition:

$$[p_d] = -[\rho] \mathbf{g} \cdot \mathbf{x}. \quad (7)$$

The dynamic boundary condition is obtained by neglecting surface tension effects and using the pressure decomposition given by Eqn. (3).

- Additional dynamic boundary condition:

$$\left[ \frac{\nabla p_d}{\rho} \right] = \mathbf{0}, \quad (8)$$

follows from the inspection of Navier–Stokes equations (Eqn. (1)) when one assumes the simplified form of the tangential stress balance given by Eqn. (6).

It is important to clearly state that the jump conditions given by Eqns. (4)–(8) have been derived with the following assumptions:

- Surface tension effects are neglected ( $\sigma = 0$ ), *i.e.* we only consider flows with high Weber numbers;
- High Reynolds number flows investigated in this work allow us to assume that the tangential stress balance is of minor importance compared to normal stress balance [24]. The kinematic viscosity is therefore defined in terms of volume fraction function [49]:

$$\nu = \alpha \nu^+ + (1 - \alpha) \nu^-, \quad (9)$$

where  $\nu^+$  is the kinematic viscosity of heavier fluid and  $\nu^-$  is the kinematic viscosity of lighter fluid.

In the VOF method, the volume fraction  $\alpha$  is defined as:

$$\alpha = \frac{V^+}{V}, \quad (10)$$

where  $V^+$  is the volume occupied by water inside a control volume  $V$ . The mass conservation equation for one phase (fluid +) reduces to the well-known VOF advection equation:

$$\frac{\partial \alpha}{\partial t} + \nabla \cdot (\mathbf{u}\alpha) = 0, \quad (11)$$

where solenoidal velocity field has been assumed, as given by Eqn. (2).

### 3. Numerical model

Continuity and Navier–Stokes equations (Eqn. (2) and Eqn. (1)) are discretised in space using a second-order accurate, collocated FV method for general unstructured/structured grids [50]. An arbitrary polyhedral control volume (CV) has a number of neighbours, each defined with surface area vector  $\mathbf{s}_j$  and distance vector  $\mathbf{d}_j$  from cell centre  $P$  to neighbouring cell centre  $N$ , as shown in Figure 1. The governing equations for the flow field (Eqn. (2) and Eqn. (1)) and the free surface advection equation (Eqn. (11)) constitute a nonlinear system of coupled partial differential equations. The pressure–velocity–free surface coupling is achieved using a combination of SIMPLE [51] and PISO [52] algorithms, where a number of PISO correctors can be used within each SIMPLE (nonlinear, or outer) correction step to ensure faster convergence without relaxation factors, as discussed by Vukčević *et al.* [25]. The continuity equation is used to derive a dynamic pressure equation using the Rhie–Chow interpolation [53] as a filter for spurious pressure oscillations. Time derivative term in the Navier–Stokes equations is discretised using a second-order accurate, two-time levels backward Euler scheme (see *e.g.* Queutey and Visonneau [23] or Tuković and Jasak [54]). The convection term is discretised using the Gauss theorem, where the face values are obtained with second-order accurate linear upwind scheme [50]. The diffusion term is discretised using the Gauss theorem and central differencing, where the non-orthogonal correction is treated using the over-relaxed approach in an explicit manner [50, 55]. The pressure gradient term in the Navier–Stokes equations and the pressure Laplacian resulting from the continuity equation are discretised using the Gauss theorem, where interface-corrected interpolation schemes take into account the jump conditions at the free surface with the Ghost Fluid Method. The reader is referred to Jasak [50] and Ferziger and Perić [56] for the details regarding polyhedral FV discretisation and the solution algorithms. The combined solution algorithm is presented in Figure 2. The next section is devoted to interface-corrected interpolation for dynamic pressure which has discontinuities across the free surface given by Eqn. (7) and Eqn. (8).

The introduction of waves in the computational domain and prevention of their reflection on outgoing boundaries is achieved with relaxation zones as introduced by Jacobsen *et al.* [12]. In Jacobsen’s approach, a part of the computational domain is dedicated to relaxation zones where the CFD solution is gradually forced towards a target solution with a smoothly varying exponential blending function. In the present study, the target solution is the potential flow solution for an incident wave. Using relaxation zones that are long enough (usually one and a half of the dominant wave length, [38]) ensures negligible wave reflection. In the present work, the volume fraction is blended explicitly with the target solution after the transport due to geometrically reconstructed advection, while the momentum equation is blended implicitly as described by Jasak *et al.* [57]. Specific settings for each of the test cases will be given, while the reader is referred to Jacobsen *et al.* [12], Jasak *et al.* [57] and Vukčević *et al.* [49] for additional details.

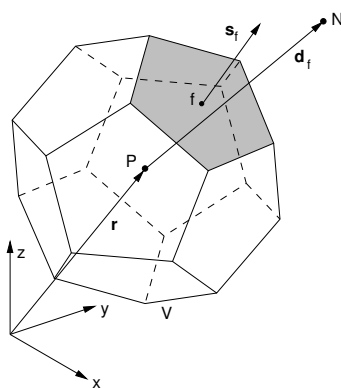


Figure 1: Polyhedral control volume. Control volume  $P$  shares a common face with its immediate neighbour  $N$ .

### 3.1. Interface-corrected dynamic pressure interpolation with the Ghost Fluid Method

One of the fundamental steps in the collocated FV method is the interpolation of fields from cell centres to face centres. Linear interpolation (or central differencing), based on Taylor series expansion becomes erroneous in presence of a discontinuity, since the expansion assumes sufficiently smooth spatial variation ( $C^1$  continuity). This can be easily demonstrated in a simplified, one-dimensional case presented in Figure 3a, where  $P$  and  $N$  denote cell centres,  $f$  is the face between them and  $\Gamma_f$  represents the interface where the discontinuity in  $\phi$  and  $\nabla\phi$  is present. Simple linear interpolation of cell centred values  $\phi_P$  and  $\phi_N$  to face centred value  $\phi_f$  yields an incorrect value since the discontinuity is not taken into account. The idea behind the GFM is to use one-sided extrapolates to define "ghost" values at the other side of the interface by second-order accurate discretisation of interface jump conditions. Since two equations (Eqn. (7) and Eqn. (8)) for dynamic pressure discontinuities exist, one can introduce two additional unknowns:  $p_d^+$  and  $p_d^-$ , infinitesimally close to the free surface from both sides. These values can be solved for and expressed in

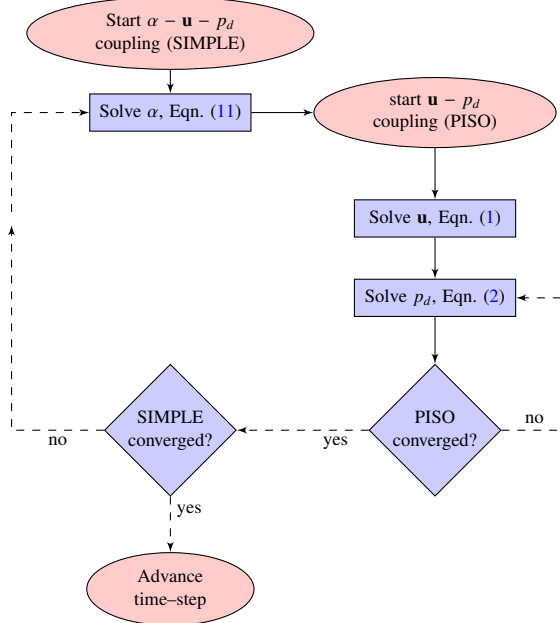


Figure 2: Flow chart of the segregated solution algorithm.

terms of cell-centred values (*i.e.*  $p_d^+ = p_d^+(p_{dN}, p_{dP})$ ), providing correct gradients. Using the correct gradients, the second-order extrapolation from the interface towards the neighbouring cell centre is carried out. This procedure is presented in Figure 3b for a general discontinuous variable  $\phi$ , defining one-sided extrapolates respecting the jump conditions at the interface. It is important to stress that no assumption has been made so far on the location of the interface.

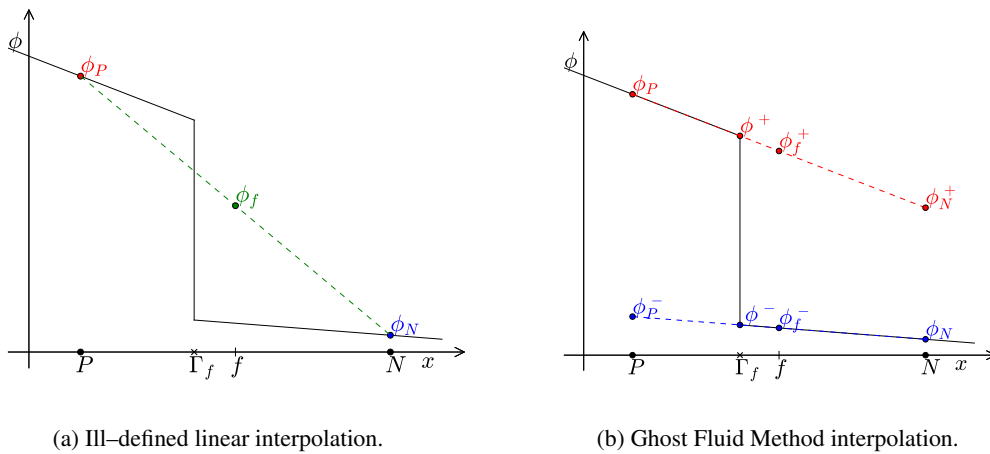


Figure 3: Cell centre to face centre interpolation schemes in the presence of a discontinuity at the interface.  $f$  is the face between cells  $P$  and  $N$  and  $\Gamma_f$  is the location of the interface (discontinuity).



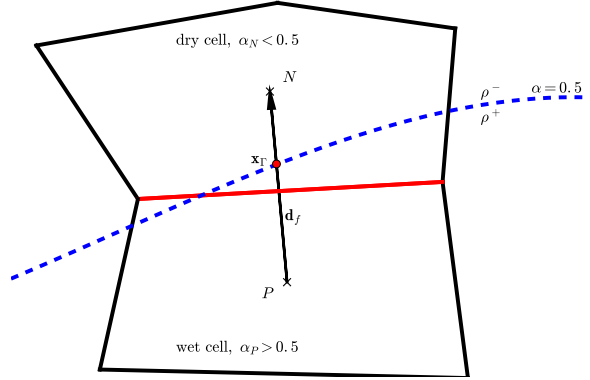


Figure 4: Unstructured interface stencil in two-dimensions [25].

The GFM interpolation is only required in the presence of discontinuities, while far from the free surface, ordinary interpolation is sufficiently accurate. In the following analysis, we assume that the free surface location can be readily estimated from the volume fraction field, provided that it remains sharp (see Sec. 3.2).

Consider a computational stencil on polygonal two-dimensional mesh for clarity, Figure 4. The free surface, denoted by blue dashed line is defined with volume fraction contour  $\alpha = 0.5$ . Cells with  $\alpha > 0.5$  are marked as "wet cells", while the cells with  $\alpha < 0.5$  are marked as "dry cells".  $\mathbf{x}_\Gamma$  represents the location of the interface somewhere along the distance vector  $\mathbf{d}_f$  between adjacent cell centres. The exact location of the interface between  $P$  and  $N$  can be defined as:

$$\mathbf{x}_\Gamma = \mathbf{x}_P + \lambda \mathbf{d}_f, \quad (12)$$

where the parametrised distance to the interface  $\lambda$  can be readily estimated using the volume fraction [25]:

$$\lambda = \frac{\alpha_P - 0.5}{\alpha_P - \alpha_N}. \quad (13)$$

Note that such procedure of defining the location of the interface does not require reconstruction using the Level Set signed distance field [24]. Formally, the location estimate given by Eqn. (13) is of the same order of accuracy as the advection step.

Before discretising the jump conditions at the interface, we introduce a substitution for the inverse density following Huang *et al.* [24]:

$$\beta = \frac{1}{\rho}. \quad (14)$$

The dynamic pressure jump conditions, written in terms of inverse density  $\beta$  reads:

$$\begin{aligned} [p_d] &= p_d^- - p_d^+ = \left( \frac{1}{\beta^-} - \frac{1}{\beta^+} \right) \mathbf{g} \cdot \mathbf{x}_\Gamma \\ &= \mathcal{H}, \end{aligned} \quad (15)$$

After the advection step, the location of the interface is calculated for each pair of interface cells using Eqn. (12). The jump in dynamic pressure can then be evaluated explicitly using Eqn. (15).

Following Huang *et al.* [24] and previous work by Vukčević *et al.* [25], the dynamic pressure gradient jump condition is discretised in a second-order accurate manner using one-sided gradient evaluations based on parametrised distance to the interface Eqn. (13):

$$\begin{aligned} [\beta \nabla p_d] &= \beta^- (\nabla p_d)^- - \beta^+ (\nabla p_d)^+ \\ &= \beta^- \frac{p_{dN} - p_d^-}{1 - \lambda} - \beta^+ \frac{p_d^+ - p_{dP}}{\lambda} = 0. \end{aligned} \quad (16)$$

The system of equations given by discretised jump conditions (Eqn. (15) and Eqn. (16)) can be easily solved for  $p_d^+$  and  $p_d^-$ . Here, the complete procedure for extrapolation is presented for cell  $P$  using  $p_d^+$ , while the procedure for cell  $N$  using  $p_d^-$  is analogous and can be easily inferred.

$$p_d^+ = \frac{\lambda \beta^-}{\beta_w} p_{dN} + \frac{(1 - \lambda) \beta^+}{\beta_w} p_{dP} - \frac{\lambda \beta^-}{\beta_w} \mathcal{H}, \quad (17)$$

where  $\overline{\beta_w}$  is the weighted inverse density:

$$\overline{\beta_w} = \lambda \beta^- + (1 - \lambda) \beta^+. \quad (18)$$

It is interesting to note that  $\overline{\beta_w}$  actually represents the harmonic interpolation of density based on the actual distance to the free surface. Once the  $p_d^+$  is known, the dynamic pressure field is extrapolated from the heavier fluid (fluid "++") at the location infinitesimally close to the free surface, towards the neighbouring cell centre:

$$p_{dN}^+ = p_d^+ + \frac{1 - \lambda}{\lambda} (p_d^+ - p_{dP}). \quad (19)$$

Substituting Eqn. (17) into Eqn. (19) yields the extrapolated value at the neighbouring cell centre given in terms of two cell centred values, inverse density and the explicit jump term  $\mathcal{H}$ :

$$p_{dN}^+ = \frac{\beta^-}{\beta_w} p_{dN} + \left( 1 - \frac{\beta^-}{\beta_w} \right) p_{dP} - \frac{\beta^-}{\beta_w} \mathcal{H}, \quad (20)$$

Eqn. (20) (and analogous expression for  $p_{dp}^-$ ) are used whenever the discretisation requires cell-centred values from the other side of the interface. The jump conditions at the free surface are therefore taken into account for the pressure gradient in the Navier–Stokes equations (Eqn. (1)) and the pressure Laplacian in the continuity equation (Eqn. (2)). The procedure has been derived using a compact computational stencil, respecting the collocated FV framework with face-based connectivity [50]. This procedure results in a symmetric discretisation of the Laplacian operator, thus preserving the symmetry of the underlying differential operator. This has been discussed in detail by Vukčević *et al.* [25], while in-depth derivation of the procedure is presented by Vukčević [49], and shall not be repeated here.

The proposed method belongs to a family of balanced force methods (see *e.g.* [58]), where the coupling between density field and dynamic pressure is resolved within the pressure equation instead of the momentum equation. The procedure assumes a priori known location of the interface defined by the volume fraction field  $\alpha$ , making it suitable for segregated (or partitioned) solution algorithms as the one used in this work (see Figure 2). The method presented so far is at most second-order accurate, although the accuracy will directly depend on the accuracy of the advection step, Eqn. (13). The next section is devoted to second-order accurate advection of the free surface.

### 3.2. Interface advection with the *isoAdvect* scheme

The implicit representation of a fluid interface via volume fractions is the natural one in the FV framework. The task of advancing the interface in time becomes a matter of modelling the composition (heavy and light fluid) of the total volume of fluid passing from one cell into its neighbour during a time step. Typically, the available information consists of volume fractions in cells at the beginning of the time step,  $\alpha_p$ , and the velocity field represented in two ways, namely by the cell averaged velocity,  $\mathbf{u}_p$ , and by the volumetric face flux,  $\phi_f$ . These velocity field representations are available at the beginning of the time step (see Figure 2), and since the nonlinear (outer) iterations are performed, we may also have estimates for them at the end of the time step. The challenge of advecting the fluid interface becomes a question of using  $\alpha_p(t)$ ,  $\mathbf{u}_p(t)$  and  $\phi_f(t)$ , and possibly available estimates of  $\mathbf{u}_p(t + \Delta t)$  and  $\phi_f(t + \Delta t)$ , to predict  $\alpha_p(t + \Delta t)$ . In the following, we will describe how this task is performed using the *isoAdvect* algorithm by Roenby *et al.* [29].

The starting point of *isoAdvect* is the continuity equation for the density field integrated over the volume of an interface cell:

$$\frac{d}{dt} \int_V \rho(\mathbf{x}, t) dV + \sum_f \int_{S_f} \rho(\mathbf{x}, t) \mathbf{u}(\mathbf{x}, t) \cdot d\mathbf{S} = 0. \quad (21)$$

Here  $V$  is the cell volume,  $S_f$  is the surface of one of the faces comprising the cell boundary and the sum  $\sum_f$  is over

all the cell's faces. Without loss of generality, define a normalised and shifted density field, or indicator function as:

$$H(\mathbf{x}, t) = \frac{\rho(\mathbf{x}, t) - \rho^-}{\rho^+ - \rho^-}, \quad (22)$$

where  $\rho^-$  and  $\rho^+$  are considered constant. Isolating  $\rho(\mathbf{x}, t)$  in Eqn. (22) and inserting it into Eqn. (21), after some rearrangement it follows:

$$\frac{d}{dt} \int_V H(\mathbf{x}, t) dV + \sum_f \int_{S_f} H(\mathbf{x}, t) \mathbf{u}(\mathbf{x}, t) \cdot d\mathbf{S} = -\frac{\rho^-}{\rho^+ - \rho^-} \sum_f \int_{S_f} \mathbf{u}(\mathbf{x}, t) \cdot d\mathbf{S}. \quad (23)$$

So far no assumption of incompressibility has been made. Assuming two constants  $\rho^+$  and  $\rho^-$  are indeed the densities of the heavy and light fluid, respectively, then both fluids are incompressible, causing the right hand side in Eqn. (23) to vanish. The indicator function,  $H(\mathbf{x}, t)$ , becomes a 3-dimensional Heaviside function taking the values 0 and 1 in the region of space occupied by the light and the heavy fluid, respectively. With the definitions of the volume fraction of cell  $P$ :

$$\alpha_P = \frac{1}{V_P} \int_{V_P} H(\mathbf{x}, t) dV, \quad (24)$$

Eqn. (23) can be written as:

$$\frac{d\alpha_P}{dt} + \frac{1}{V_P} \sum_f \int_{S_f} H(\mathbf{x}, t) \mathbf{u}(\mathbf{x}, t) \cdot d\mathbf{S} = 0. \quad (25)$$

This equation is exact for incompressible fluids. The key to accurate interface advection is to realise that the discontinuous nature of the problem demands geometric modelling involving considerations of the shape and orientation of the face, as well as of the local position, orientation and motion of the interface. We formally integrate Eqn. (25) over time from time  $t$  to time  $t + \Delta t$ :

$$\alpha_P(t + \Delta t) = \alpha_P(t) - \frac{1}{V_P} \sum_f \Delta V_f(t, \Delta t) \quad (26)$$

where  $\Delta V_f(t, \Delta t)$  denotes the volume of heavy fluid transported through the face  $f$  during the time step  $[t, t + \Delta t]$ :

$$\Delta V_f(t, \Delta t) = \int_t^{t+\Delta t} \int_f H(\mathbf{x}, \tau) \mathbf{u}(\mathbf{x}, \tau) \cdot d\mathbf{S} d\tau. \quad (27)$$

If the flow was steady and face  $f$  completely immersed in the heavy fluid during the entire time step, this will just be  $\Delta V_f(t, \Delta t) = \phi_f \Delta t$ . Likewise, if the face was in the light fluid throughout the time step,  $\Delta V_f(t, \Delta t)$  would be zero. But even for steady flows, some faces will in general be fully or partially swept by the interface in a non-trivial manner during a time step. In the `isoAdvect` advection step we model the face-interface intersection line sweeping the

face during the time step. This approach is geometric in nature, but novel compared to existing geometric advection methods that focus on calculation of flux polyhedra and their intersection with the mesh cells [42, 39, 40, 41].

The first step in our modelling process is to realise that the rapid changes in  $\Delta V_f$  during a time step is typically not due to an abruptly varying velocity field but due to the passage of the interface through the cell face. Hence, we will assume that  $\mathbf{u}(\mathbf{x}, \tau) \cdot d\mathbf{S}$  in Eqn. (27) can be written in terms of an averaged flux over the face and over the time step:

$$\mathbf{u}(\mathbf{x}, \tau) \cdot d\mathbf{S} \approx \bar{\mathbf{u}}_f \cdot \mathbf{n}_f dA = \frac{\bar{\phi}_f}{A_f} dA, \text{ for } \mathbf{x} \in S_f \text{ and } t \in [t, t + \Delta t]. \quad (28)$$

Here  $\bar{\mathbf{u}}_f$  and  $\bar{\phi}_f$  can be thought of as averages over both time step and face area. At the beginning of the algorithm, stepping forward from time  $t$ , we may use the available  $\phi_f(t)$  as the estimate of the average flux over the time step,  $\bar{\phi}_f$ . However, during nonlinear iterations in a single time step, the averaged flux is readily available due to the availability of  $\phi_f(t + \Delta t)$ . In any case, inserting Eqn. (28) into Eqn. (27) we can write:

$$\Delta V_f(t, \Delta t) \approx \bar{\phi}_f \int_t^{t+\Delta t} \alpha_f^+(\tau) d\tau, \quad (29)$$

where we have defined the quantity:

$$\alpha_f^+(t) = \frac{1}{A_f} \int_f H(\mathbf{x}, t) dA, \quad (30)$$

which is the instantaneous ‘‘Area-Of-Fluid’’ of face  $f$ , i.e. the fraction of the face area submerged in heavy fluid. If the velocity field is constant in space and time and the face is planar, the approximation in Eqn. (29) becomes exact.

To progress, we now assume that the interface has been reconstructed within the interface cell from which face  $f$  receives fluid (upwind cell). The reconstructed interface is represented by an internal polygonal face. We will call such a cell cutting face an *isoface*, for reasons to become clear below. The isoface cuts the cell into two disjoint sub-cells occupied by the heavy and light fluid, respectively, as illustrated in [Figure 5a](#).

The isoface will intersect some cell faces, cutting them into two subfaces immersed in heavy and light fluid, respectively, while others will be fully immersed in one of the two fluids. This is the state at time  $t$ . However, Eqn. (29) requires  $\alpha_f^+$  for the whole interval  $[t, t + \Delta t]$ . To obtain an estimate of this, we first note that the isoface will have a well-defined face centre,  $\mathbf{x}_S$  and a well defined unit normal,  $\mathbf{n}_S$ , the latter by convention pointing away from the heavy fluid. We may then interpolate the cell averaged velocity field,  $\mathbf{u}_P$  to the isoface centre,  $\mathbf{x}_S$ , to obtain the isoface velocity  $\mathbf{u}_S$ . If the fluid interface is a plane with unit normal  $\mathbf{n}_S$  starting at  $\mathbf{x}_S$  at time  $t$  and moving with

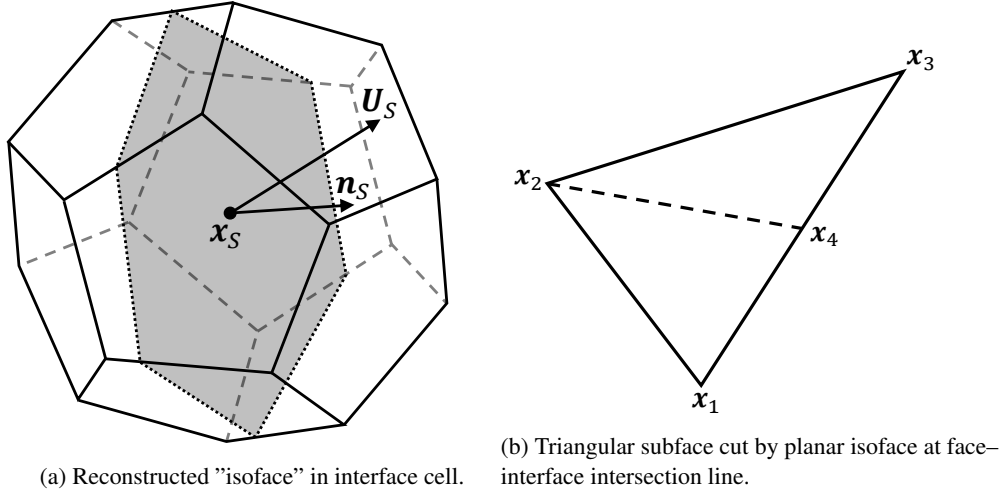


Figure 5: Reconstructed isoface within a polyhedral cell.

constant velocity  $\mathbf{u}_S$ , then the interface will arrive at a given point  $\mathbf{x}_v$  at time:

$$t_v = t + \frac{(\mathbf{x}_v - \mathbf{x}_S) \cdot \mathbf{n}_S}{\mathbf{u}_S \cdot \mathbf{n}_S}. \quad (31)$$

In particular, this holds true for all points on the general polygonal ( $N$ -sided) face  $f$ , including its vertices  $\mathbf{x}_1, \dots, \mathbf{x}_N$ , and therefore defines the face-interface intersection line at any  $\tau \in [t, t + \Delta t]$  as required in Eqn. (29). We will now use this to explicitly calculate the time integral in Eqn. (29).

First note that a planar polygonal face may be triangulated in a number of ways, with the triangles lying exactly on the surface of the face. For a non-planar polygonal face we must define its surface, which we do by estimating a face centre and using that as the apex for  $N$  triangles with the  $N$  face edges as base lines. The face surface is then defined by the union of these  $N$  triangles. In other words, any polygonal face may be represented as a union of triangles. Our analysis can therefore be confined to a triangular subface since the contribution from these can subsequently be accumulated to obtain the time integral in Eqn. (29) for the whole face. Therefore, we consider a triangle with vertices  $\mathbf{x}_1, \mathbf{x}_2$  and  $\mathbf{x}_3$ . The interface arrival times from Eqn. (31) can be calculated and we may assume without loss of generality that the points are ordered such that  $t_1 \leq t_2 \leq t_3$ . The interface enters the triangle at time  $t_1$  at the point  $\mathbf{x}_1$ , and then sweeps the triangle reaching  $\mathbf{x}_2$  at time  $t_2$ , where it also intersects the edge  $\mathbf{x}_1 - \mathbf{x}_3$  at a point we shall call  $\mathbf{x}_4$ , illustrated in Figure 5b. In what follows, we denote an edge between  $\mathbf{x}_i$  and  $\mathbf{x}_j$  as  $\mathbf{x}_{ij} = \mathbf{x}_i - \mathbf{x}_j$ . Then for  $\mathbf{x}_4$  we have:

$$\mathbf{x}_4 = \frac{\mathbf{x}_{21} \cdot \mathbf{n}_S}{\mathbf{x}_{31} \cdot \mathbf{n}_S} \mathbf{x}_{31}. \quad (32)$$

Finally, at time  $t_3$ , the interface leaves the face through  $\mathbf{x}_3$ . We note that in general the three times  $t_1$ ,  $t_2$  and  $t_3$  and the two times  $t$  and  $t + \Delta t$  can be distributed in various ways. For instance if  $t < t_1 < t_2 < t + \Delta t < t_3$ , then the triangle is completely immersed in the light fluid from time  $t$  to time  $t_1$  at which point the isoface will enter the triangle sweeping it and ending up at time  $t + \Delta t$  on the triangle. The correct ordering must be taken into account, when doing the time integration in Eqn. (29). Let us for the sake of simplicity consider the case where the triangle is entirely swept during the time step, i.e. where  $t < t_1$  and  $t_3 < t + \Delta t$ . We will derive an expression for  $\alpha^+(\tau)$  under the assumption that  $\mathbf{U}_s \cdot \mathbf{n}_s > 0$ , meaning that the interface is moving towards the light fluid region within the cell. If this is not the case, what we have derived is instead an expression for  $1 - \alpha^+$ , which is equally useful. At a time  $\tau$  between  $t_1$  and  $t_2$ , the immersed part of the triangle will have area:

$$A^+(\tau) = \frac{1}{2} |\mathbf{x}_{41} \tilde{t} \times \mathbf{x}_{21} \tilde{t}| \quad \text{where} \quad \tilde{t} = \frac{\tau - t_1}{t_2 - t_1}. \quad (33)$$

With a total area of the triangle of  $A = \frac{1}{2} |\mathbf{x}_{31} \times \mathbf{x}_{21}|$ , we can then write:

$$\alpha^+(\tau) = \frac{|\mathbf{x}_{41} \times \mathbf{x}_{21}|}{2A} \left( \frac{\tau - t_1}{t_2 - t_1} \right)^2 \quad \text{for} \quad t_1 < \tau < t_2. \quad (34)$$

In a similar manner we find:

$$\alpha^+(\tau) = \alpha^+(t_2) + \frac{|\mathbf{x}_{43} \times \mathbf{x}_{23}|}{2A} \left[ 1 - \left( 1 - \frac{\tau - t_3}{t_2 - t_3} \right)^2 \right] \quad \text{for} \quad t_2 < \tau < t_3. \quad (35)$$

From Eqn. (34) and Eqn. (35) it is evident that  $\alpha^+$  for the sub-triangles of a polygonal face are quadratic polynomials in  $\tau$  with coefficients changing at the intermediate time  $t_2$ . The coefficients are uniquely determined by the face vertex positions,  $\mathbf{x}_1$ ,  $\mathbf{x}_2$  and  $\mathbf{x}_3$ , the isoface velocity,  $\mathbf{u}_s$ , the unit normal,  $\mathbf{n}_s$ , and the isoface centre at the beginning of the time step,  $\mathbf{x}_s$ . In Figure 6a and Figure 6b, we show an example of the time evolution of  $\alpha_f^+(t)$  for a polygonal face as it is swept by a planar interface.

If we call the polynomial coefficients for the first sub time interval of an polygon's  $i$ 'th triangle  $A_{i,1}$ ,  $B_{i,1}$  and  $C_{i,1}$  (see Eqn. (34)), and the coefficients for its second sub interval  $A_{i,2}$ ,  $B_{i,2}$  and  $C_{i,2}$  (see Eqn. (35)), then the time integral in Eqn. (29) takes the form:

$$\int_t^{t+\Delta t} \alpha_f^+(\tau) d\tau \approx \sum_{i=1}^N \sum_{j=1}^2 \frac{1}{3} A_{i,j} (t_{i,j+1}^3 - t_{i,j}^3) + \frac{1}{2} B_{i,j} (t_{i,j+1}^2 - t_{i,j}^2) + C_{i,j} (t_{i,j+1} - t_{i,j}). \quad (36)$$

Here  $t_{i,1}$ ,  $t_{i,2}$  and  $t_{i,3}$  are the arrival times for the  $i$ 'th triangle of our polygonal face (see Eqn. (31)). The approximation

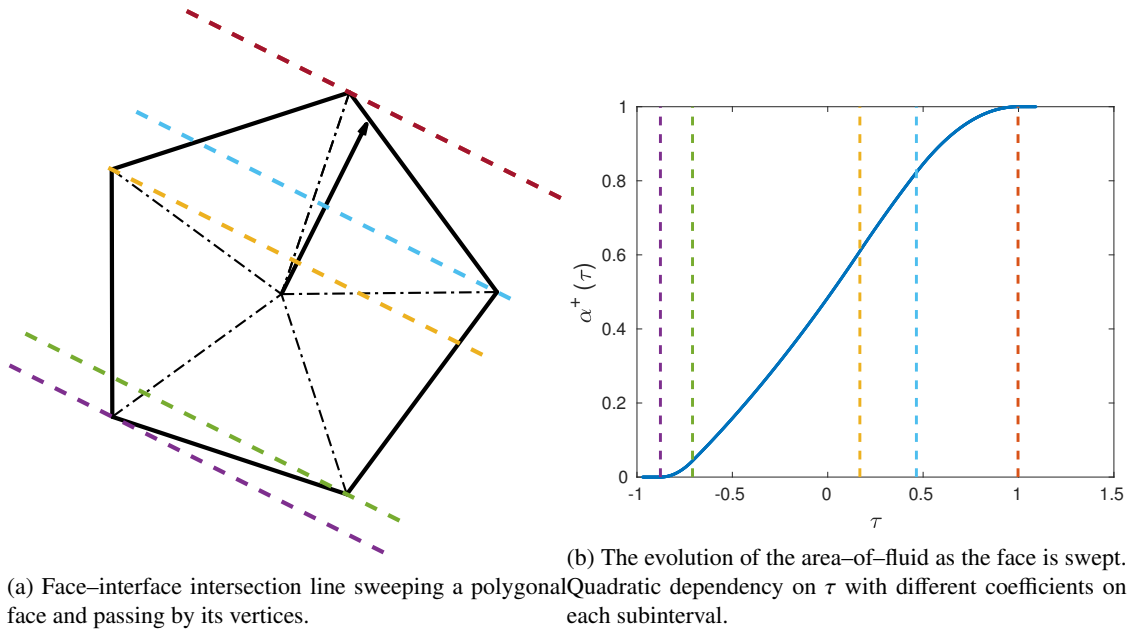


Figure 6: `isoAdvecting` algorithm sweeping a polygonal face.

in Eqn. (36) is exact if the interface is in fact a plane with normal  $\mathbf{n}_S$  starting at position  $\mathbf{x}_S$  at time  $t$  and travelling with constant velocity  $\mathbf{u}_S \cdot \mathbf{n}_S$  normal to itself.

This concludes our description of the `isoAdvecting` advection step. We will now briefly describe the `isoAdvecting` reconstruction step giving rise to the first syllable, the "iso", in the method name. The reconstruction step is used to obtain the isoface at the beginning of a time step including its centre  $\mathbf{x}_S$  and unit normal,  $\mathbf{n}_S$ . As suggested by the name, this is done by representing the isoface as the intersection between the cell and a numerically calculated isosurface of the volume fraction field,  $\alpha_P(t)$ . To calculate such isosurface, the volume fraction field is first interpolated from the cell centres to the vertices of the cell. In the current implementation the inverse centre-to-vertex distances are used as interpolation weights. With a volume fraction value associated with each cell vertex, we can now for a given iso–value,  $\alpha_0$ , determine for each cell edge, if  $\alpha_0$  lies between the two vertex values of that edge. If this is the case, we mark a cut point on the edge by linear interpolation. Doing this for all the cell's edges and connecting the cut points across the cell faces, we obtain the isoface. Its centre and normal can be calculated by triangulation as for any other polygonal face.

It is important to choose for each interface cell a distinct iso–value giving rise to an isoface cutting the cell into sub–cells of volumetric proportions in accordance with the volume fraction of the cell. The search algorithm for finding the iso–value to within a user specified tolerance has been optimized by exploiting the known functional form of a subcell volume as a function of the iso–value. For more details, the reader is referred to Roenby *et al.* [29].



The final element in the `isoAdvect` algorithm is a heuristic bounding step. It is introduced to correct volume fractions ending up outside the meaningful interval,  $[0, 1]$ , if the `isoAdvect` algorithm is stressed beyond its formal region of validity by taking time steps so large that the underlying geometric assumptions break down. The bounding step is optional and contains both a volume-preserving step and an optional non-conservative brute force chopping of the volume fractions. For more details, the reader is referred to Roenby *et al.* [29].

The advection step presented in this section is formally second order accurate since the time-averaged velocity and volumetric flux fields,  $\bar{\mathbf{u}}_f$  and  $\bar{\phi}_f$  field, respectively, are used. This corresponds to a well-known Crank–Nicolson scheme.

#### 4. Test cases

This section presents verification and validation of the proposed numerical approach. The analysis starts by considering a progressive wave using a set of uniformly refined grids to calculate numerical uncertainty and achieved order of convergence. In addition, the results are compared with stream function wave theory based on potential flow solution [59]. Finally, we consider wave impact loads on a deck of a simplified ship in regular waves, comparing the results with recent experimental data, while also assessing numerical uncertainty for the pressure impulses. This wave breaking phenomena is often denoted as the "green–water effect".

##### 4.1. Wave propagation

A progressive wave with parameters given in Table 1 is considered for verification purposes. The wave is moderately nonlinear [60] with steepness  $kH/2 = 0.174$ . The computational domain is thirteen wave lengths long ( $L_x = 13\lambda$ ) and two water depths high ( $L_y = 2d$ ). Relaxation zones that are  $1.5\lambda$  long are used at the left and right boundaries to introduce waves and prevent wave reflection, while the wave propagates from left to right boundary. Such a long domain allows us to have ten wave lengths of full CFD solution unaffected by relaxation zones, which gives us the possibility to investigate the dissipation (loss of wave amplitude) and dispersion errors (phase drift) along the numerical wave tank.

Six structured, uniform grids outlined in Table 2 are used to calculate the achieved order of accuracy and numerical uncertainty using the least squares method according to Eça and Hoekstra [47, 61]. Grids 1 and 2 are obtained by coarsening Grid 3, while Grids 4, 5 and 6 are obtained by refining Grid 3. A constant refinement factor of  $r = 1.4$  has been used for both spatial dimensions and for time. Therefore, the smallest computation is performed on Grid 1 with 11 865 cells (approximately 26 cells per wave length and 5 cells per wave height) using 102 time steps per encounter

period, while the largest computation is performed on Grid 6 with 338 520 cells (approximately 140 cells per wave length and 28 cells per wave height) using 549 time steps per encounter period.

Wave elevation is measured at twelve locations,  $1\lambda, 2\lambda \dots 12\lambda$  from the inlet. A representative signal obtained using Grid 6 at wave gauge  $6\lambda$  is shown in Figure 7a, with its frequency content presented in Figure 7b. The frequency content indicates that most of the energy,  $(\eta/H)^2$  is contained within the first harmonic, while approximately 10% is contained within higher harmonics. Velocity is also measured at twelve locations corresponding to  $1\lambda, 2\lambda \dots 12\lambda$  below the calm free surface at  $z = -0.3$  metres. The locations of the velocity probes are presented in Figure 8. The initial condition for the simulation corresponds to the solution from the stream function wave theory [59].

#### 4.1.1. Verification analysis for the progressive wave

Eça *et al.* [62] have recently shown that the iterative errors in unsteady simulations should be kept to a minimum, otherwise they can significantly influence the final solution. Therefore, all simulations are performed with six nonlinear

Table 1: Progressive wave parameters.

Wave height	$H$ , m	0.3
Wave period	$T$ , s	2
Wave radian frequency	$\omega$ , rad/s	$\pi$
Wave length	$\lambda$ , m	5.409
Water depth	$d$ , m	1
Wave steepness	$kH/2$	0.174

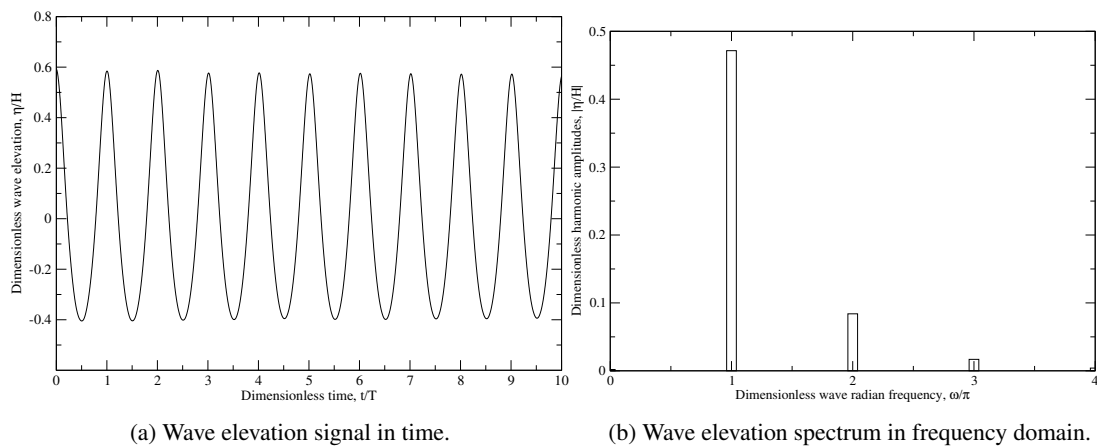


Figure 7: Wave elevation at wave gauge  $6\lambda$  obtained with Grid 6.

Table 2: Grids for the wave propagation case.

Grid index	1	2	3	4	5	6
Number of cells	11 865	23 226	45 084	88 160	172 900	338 520
Number of time steps per wave period	102	143	200	280	392	549
Number of cells per wave length	26	37	51	71	100	140
Number of cells per wave height	5.2	7.3	10.2	14.3	20.0	28.0



Figure 8: Location of the velocity probes and wave gauges.

iterations per time step and two additional pressure correction steps per each nonlinear iteration. Relaxation is not used. The settings ensure that residuals for all variables measured by the  $L_1$  norm in the last nonlinear iteration are always smaller than  $5 \times 10^{-6}$ , making iterative uncertainty small. The residuals during the simulations have oscillatory behaviour, [Figure 9](#), while on average they are approximately  $\mathcal{O}(10^{-9})$ .

**Verification study for first order effects.** Achieved order of spatial  $p$  and temporal  $q$  convergence of first order amplitude of wave elevation,  $\eta_A$  is presented in [Figure 10](#) following the guidelines by Eça and Hoekstra [47] and using their open access tool [61]. The achieved orders of spatial and temporal accuracy range from 0.54 to 2.00, while the average value for all wave gauges is 1.30. Average numerical uncertainty for the fine grid  $\eta_U$  is 2.25% considering all wave gauges. The achieved order of accuracy is lower further downstream of the numerical wave tank, and consequently numerical uncertainty for the fine grid  $U_{\eta_A}$  is larger. This trend is presented in [Figure 10b](#). From previous experience with wave-related problems in ocean and marine engineering, it is sufficient to consider only a few wave lengths in the computational domain [37, 49]. If only the first five wave lengths were considered, the average order

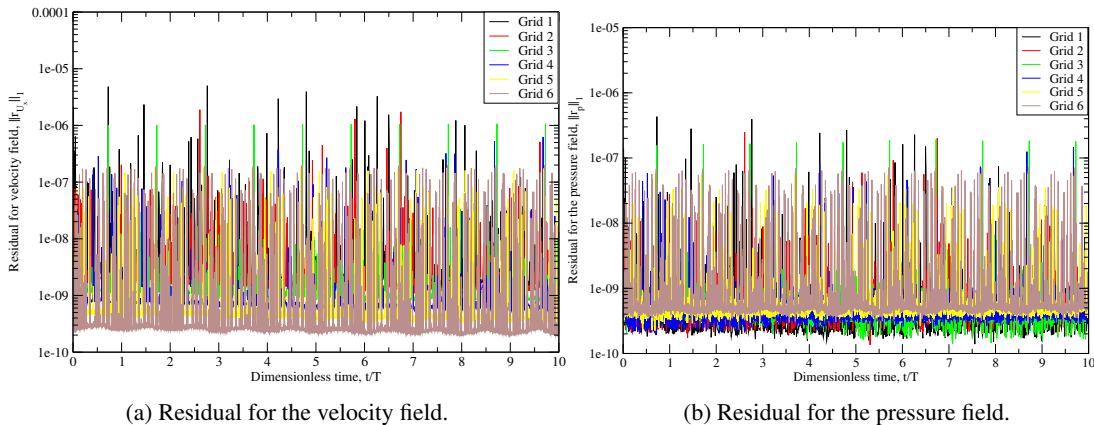


Figure 9:  $L_1$  residuals during the simulations, indicating the level of iterative convergence used in present simulations.

of accuracy would be 1.64 for space and 1.63 for time. Consequently, the average numerical uncertainty for first five wave lengths is 0.6%, compared to 2.25% for all wave lengths. In addition, the second column of Figure 10 presents the guessed asymptotic solution for each of wave gauges, where the average first order amplitude is 0.142 metres.

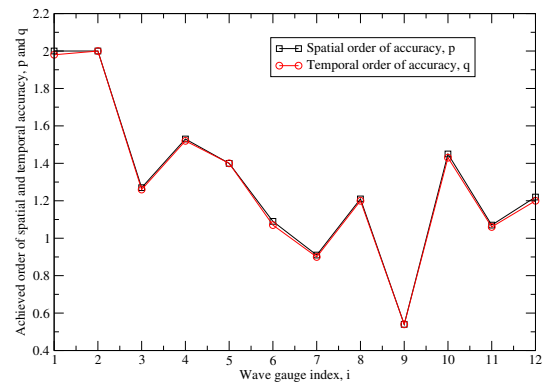
Figure 11 presents verification analysis for first order harmonic phases,  $\eta_\theta$ . The achieved orders of spatial and temporal accuracy range from 1.23 to 2.00, with average values 1.86 for space and 1.91 for time. Better convergence with refinement is thus obtained for first order harmonic phases compared to first order harmonic amplitudes. The dispersion error (error in phase) is well-behaved compared to the dissipation error (error in amplitude), although more studies should be carried out to draw more general conclusions. Achieved spatial and temporal orders of convergence are well-behaved for all wave gauges as presented in Figure 11b, except for the outlier at wave gauge 5 that measured low order of spatial convergence. Numerical uncertainties on Grid 6 for the phases are presented in degrees in the third column of Figure 11, with average of approximately 4°.

Figure 12 presents the results of the verification analysis for the first order amplitude of  $x$  (horizontal) component of the velocity field,  $u_{xA}$ . Averaged for all probes,  $u_{xA}$  exhibits convergence with grid and time step refinement of 1.69 and 1.62, respectively. Here, a single ill-behaved convergence has been observed where a fit was made using first and second order exponents following Eça and Hoekstra [47]. The convergence shows irregular behaviour for different probes. The associated numerical uncertainties on the fine grid are lower than 3.5%, except for the two outliers at probes 3 and 4 with high numerical uncertainties of 12% and 15.5%, respectively.

Figure 13 presents the results for the first order phase of  $x$  component of the velocity field,  $u_{x\theta}$ . Achieved order of spatial accuracy and temporal accuracy is 1.53 and 1.61, respectively, averaged over all probes. The associated

Item	$\eta_A$ , m	$U_{\eta_A}$	$p$	$q$
$\eta_{AG1}$	$1.44 \times 10^{-1}$	0.4%	2.00	1.98
$\eta_{AG2}$	$1.43 \times 10^{-1}$	0.5%	2.00	2.00
$\eta_{AG3}$	$1.42 \times 10^{-1}$	0.4%	1.27	1.26
$\eta_{AG4}$	$1.41 \times 10^{-1}$	0.6%	1.53	1.52
$\eta_{AG5}$	$1.41 \times 10^{-1}$	1.1%	1.40	1.40
$\eta_{AG6}$	$1.43 \times 10^{-1}$	3.5%	1.09	1.07
$\eta_{AG7}$	$1.42 \times 10^{-1}$	2.9%	0.91	0.90
$\eta_{AG8}$	$1.39 \times 10^{-1}$	1.2%	1.21	1.20
$\eta_{AG9}$	$1.45 \times 10^{-1}$	5.8%	0.54	0.54
$\eta_{AG10}$	$1.39 \times 10^{-1}$	1.2%	1.45	1.43
$\eta_{AG11}$	$1.41 \times 10^{-1}$	2.9%	1.07	1.06
$\eta_{AG12}$	$1.48 \times 10^{-1}$	6.6%	1.22	1.20
Average	$1.42 \times 10^{-1}$	2.25%	1.31	1.30

(a) Results for all wave gauges.

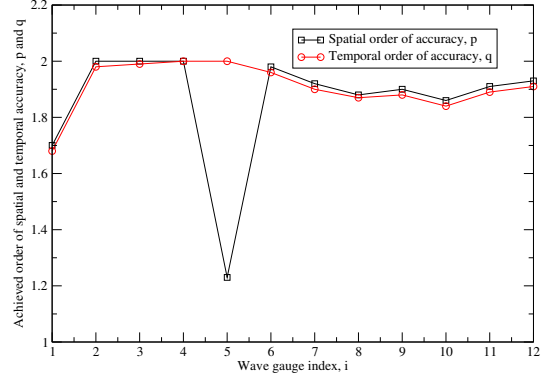


(b) Achieved order of convergence for all wave gauges.

Figure 10: Uncertainty analysis for wave elevation: first order amplitudes.

Item	$\eta_{\theta}, ^{\circ}$	$U_{\eta_{\theta}}, ^{\circ}$	$p$	$q$
$\eta_{\theta G1}$	182	0.2	1.70	1.68
$\eta_{\theta G2}$	180	0.4	2.00	1.98
$\eta_{\theta G3}$	179	1.1	2.00	1.99
$\eta_{\theta G4}$	178	1.6	2.00	2.00
$\eta_{\theta G5}$	179	4.0	1.23	2.00
$\eta_{\theta G6}$	178	5.0	1.98	1.96
$\eta_{\theta G7}$	178	5.4	1.92	1.90
$\eta_{\theta G8}$	177	5.8	1.88	1.87
$\eta_{\theta G9}$	177	6.1	1.90	1.88
$\eta_{\theta G10}$	177	6.3	1.86	1.84
$\eta_{\theta G11}$	177	6.3	1.91	1.89
$\eta_{\theta G12}$	183	4.9	1.93	1.91
Average	179	3.92	1.86	1.91

(a) Results for all wave gauges.



(b) Achieved order of convergence for all wave gauges.

Figure 11: Uncertainty analysis for wave elevation: first order phases.

numerical uncertainties range from 2.2 to 28.8°. The analysis shows irregular behaviour across all velocity probes.

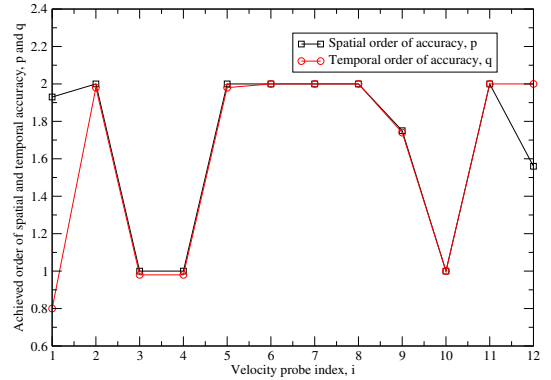
Figure 14 presents the results for the first order amplitude of  $y$  (vertical) component of the velocity field,  $u_{yA}$ . Achieved order of spatial accuracy and temporal accuracy is lower compared to wave elevation and horizontal velocity component, with average values of 1.17 and 1.10, respectively. The numerical uncertainty is lower than 3% for majority of the probes, with outliers up to 10.5%.

Figure 15 presents the results for the first order phase of  $y$  (vertical) component of the velocity field,  $u_{y\theta}$ . Achieved orders of spatial accuracy and temporal accuracy are 1.48 and 1.47, respectively, averaged over all probes. The nu-

Item	$u_{xA}, \text{ m/s}$	$U_{u_{xA}} \%$	$p$	$q$
$u_{xAP1}$	$4.10 \times 10^{-1}$	3.4%	1.93	0.80
$u_{xAP2}$	$3.98 \times 10^{-1}$	1.1%	2.00	1.98
$u_{xAP3}$	$3.60 \times 10^{-1}$	12.0%	1.00	0.98
$u_{xAP4}$	$3.46 \times 10^{-1}$	15.5%	1.00	0.98
$u_{xAP5}$	$3.89 \times 10^{-1}$	1.3%	2.00	1.98
$u_{xAP6}$	$3.94 \times 10^{-1}$	1.9%	2.00	2.00
$u_{xAP7}$	$3.93 \times 10^{-1}$	2.1%	2.00	2.00
$u_{xAP8}$	$3.92 \times 10^{-1}$	2.0%	2.00	2.00
$u_{xAP9}$	$3.88 \times 10^{-1}$	1.9%	1.75	1.74
$u_{xAP10}$	$3.88 \times 10^{-1}$	0.7%	* 1,2	1.00
$u_{xAP11}$	$3.92 \times 10^{-1}$	1.8%	2.00	2.00
$u_{xAP12}$	$4.09 \times 10^{-1}$	2.4%	1.56	2.00
Average	$3.88 \times 10^{-1}$	3.84	1.69	1.62

\* 1,2 Fit was made using first and second order exponents

(a) Results for all probes.



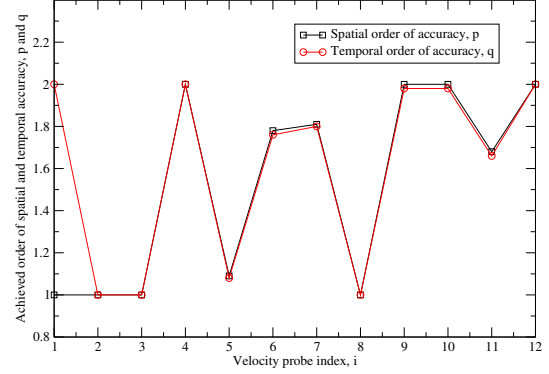
(b) Achieved order of convergence for all probes.

Figure 12: Uncertainty analysis for  $x$  (horizontal) component of the velocity field: first order amplitudes.

Item	$u_{x\theta}, ^\circ$	$U_{U_{x\theta}}, ^\circ$	$p$	$q$
$u_{x\theta P1}$	166	18.2	* 1,2	2.00
$u_{x\theta P2}$	179	2.2	1.00	* 1,2
$u_{x\theta P3}$	174	3.8	* 1,2	1.00
$u_{x\theta P4}$	180	4.1	2.00	2.00
$u_{x\theta P5}$	198	28.8	1.09	1.08
$u_{x\theta P6}$	180	12.3	1.78	1.76
$u_{x\theta P7}$	178	10.1	1.81	1.80
$u_{x\theta P8}$	173	7.4	1.00	* 1,2
$u_{x\theta P9}$	177	7.2	2.00	1.98
$u_{x\theta P10}$	178	18.2	2.00	1.98
$u_{x\theta P11}$	188	20.9	1.68	1.66
$u_{x\theta P12}$	182	6.1	2.00	2.00
<b>Average</b>	<b>179</b>	<b>11.6</b>	<b>1.53</b>	<b>1.61</b>

\* 1,2 Fit was made using first and second order exponents

(a) Results for all probes.



(b) Achieved order of convergence for all probes.

Figure 13: Uncertainty analysis for  $x$  (horizontal) component of the velocity field: first order phases.

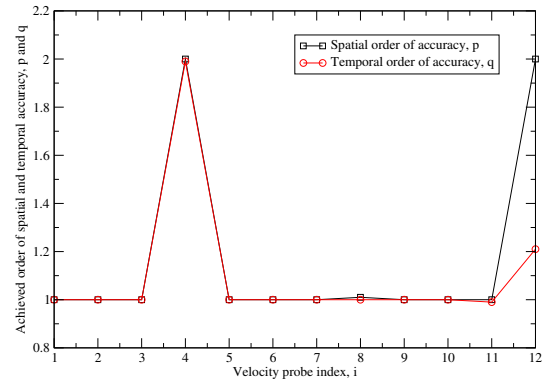
merical uncertainty is on average  $9^\circ$ .

**Verification study for second order effects.** The verification study is continued by performing the same analysis for second order effects since the wave is moderately nonlinear ( $kH/2 = 0.174$ ). Figure 16 presents verification results for second order wave elevation amplitudes. The average asymptotic solution over all wave gauges is 0.0243 metres, which is approximately five times smaller than the average first order amplitude (0.142 metres). The average uncer-

Item	$u_{yA}, \text{m/s}$	$U_{U_{yA}}, \%$	$p$	$q$
$u_{yAP1}$	$2.77 \times 10^{-1}$	1.1%	* 1,2	1.00
$u_{yAP2}$	$2.73 \times 10^{-1}$	0.3%	* 1,2	* 1,2
$u_{yAP3}$	$2.73 \times 10^{-1}$	1.2%	* 1,2	1.00
$u_{yAP4}$	$2.65 \times 10^{-1}$	1.5%	2.00	1.99
$u_{yAP5}$	$2.53 \times 10^{-1}$	6.8%	* 1,2	* 1,2
$u_{yAP6}$	$2.71 \times 10^{-1}$	2.4%	* 1,2	1.00
$u_{yAP7}$	$2.70 \times 10^{-1}$	2.0%	* 1,2	1.00
$u_{yAP8}$	$2.43 \times 10^{-1}$	10.5%	1.01	1.00
$u_{yAP9}$	$2.71 \times 10^{-1}$	2.8%	* 1,2	* 1,2
$u_{yAP10}$	$2.69 \times 10^{-1}$	1.9%	* 1,2	1.00
$u_{yAP11}$	$2.56 \times 10^{-1}$	4.6%	1.00	0.99
$u_{yAP12}$	$2.69 \times 10^{-1}$	4.9%	2.00	1.21
<b>Average</b>	<b><math>2.66 \times 10^{-1}</math></b>	<b>3.33</b>	<b>1.17</b>	<b>1.10</b>

\* 1,2 Fit was made using first and second order exponents

(a) Results for all probes.



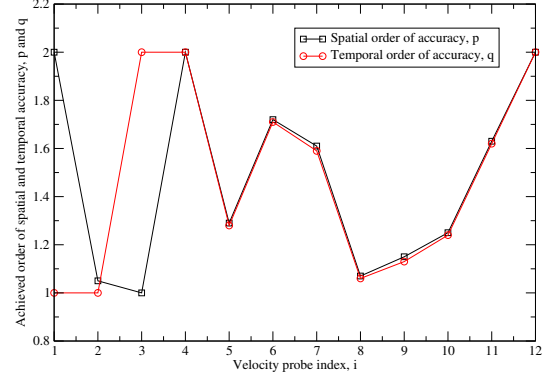
(b) Achieved order of convergence for all probes.

Figure 14: Uncertainty analysis for  $y$  (vertical) component of the velocity field: first order amplitudes.

Item	$u_{y\theta}, ^\circ$	$U_{U_{y\theta}}, ^\circ$	$p$	$q$
$u_{y\theta P1}$	256	11.3	2.00	* 1.2
$u_{y\theta P2}$	267	3.6	1.05	1.00
$u_{y\theta P3}$	278	9.2	* 1.2	2.00
$u_{y\theta P4}$	270	2.9	2.00	2.00
$u_{y\theta P5}$	278	11.7	1.29	1.28
$u_{y\theta P6}$	270	8.5	1.72	1.71
$u_{y\theta P7}$	270	7.9	1.61	1.59
$u_{y\theta P8}$	269	7.6	1.07	1.06
$u_{y\theta P9}$	277	14.0	1.15	1.13
$u_{y\theta P10}$	277	13.3	1.25	1.24
$u_{y\theta P11}$	279	14.2	1.63	1.62
$u_{y\theta P12}$	273	3.8	2.00	2.00
<b>Average</b>	<b>272</b>	<b>9.0</b>	<b>1.48</b>	<b>1.47</b>

\* 1,2 Fit was made using first and second order exponents

(a) Results for all probes.



(b) Achieved order of convergence for all probes.

Figure 15: Uncertainty analysis for  $y$  (horizontal) component of the velocity field: first order phases.

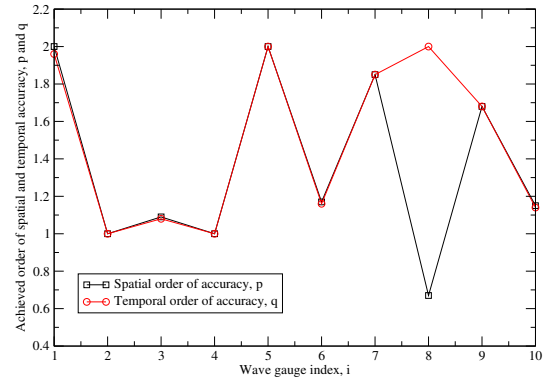
tainty is 7.81%, ranging from 0.1% to 21.3%. Achieved orders of spatial and temporal accuracy range from 0.67 to 2, with average values of 1.42 and 1.52, respectively.

Figure 17 presents the results for second order wave elevation phases. The asymptotic solution for all wave gauges is approximately  $176^\circ$ , while the corresponding numerical uncertainty is  $6.4^\circ$  on average. The achieved orders of spatial and temporal accuracy range from 0.92 to 2.00, with the average values of 1.88 and 1.89, respectively.

Item	$\eta_A, \text{m}$	$U_{\eta_A}$	$p$	$q$
$\eta_{AG1}$	$2.64 \times 10^{-2}$	0.1%	2.00	1.96
$\eta_{AG2}$	$2.45 \times 10^{-2}$	8.5%	* 1.2	* 1.2
$\eta_{AG3}$	$2.23 \times 10^{-2}$	18.8%	1.09	1.08
$\eta_{AG4}$	$2.10 \times 10^{-2}$	21.3%	* 1.2	* 1.2
$\eta_{AG5}$	$2.56 \times 10^{-2}$	7.9%	2.00	2.00
$\eta_{AG6}$	$2.30 \times 10^{-2}$	8.8%	1.17	1.16
$\eta_{AG7}$	$2.48 \times 10^{-2}$	1.8%	1.85	1.85
$\eta_{AG8}$	$2.71 \times 10^{-2}$	13.4%	0.67	2.00
$\eta_{AG9}$	$2.52 \times 10^{-2}$	3.4%	1.68	1.68
$\eta_{AG10}$	$2.35 \times 10^{-2}$	5.9%	1.15	1.14
$\eta_{AG11}$	$2.43 \times 10^{-2}$	1.6%	1.78	1.77
$\eta_{AG12}$	$2.41 \times 10^{-2}$	2.3%	1.60	1.59
<b>Average</b>	<b><math>2.43 \times 10^{-2}</math></b>	<b>7.81%</b>	<b>1.42</b>	<b>1.52</b>

\* 1,2 Fit was made using first and second order exponents

(a) Results for all wave gauges.

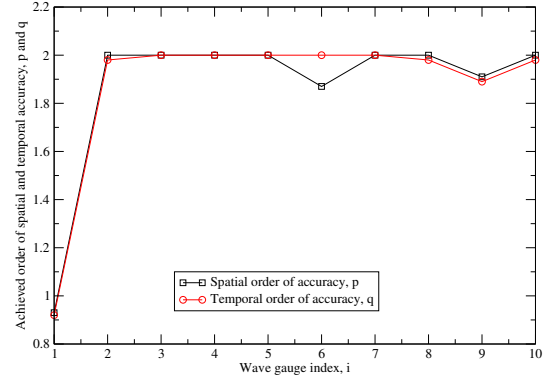


(b) Achieved order of convergence for all wave gauges.

Figure 16: Uncertainty analysis for wave elevation: second order amplitudes.

Item	$\eta_{\theta}, ^\circ$	$U_{\eta_{\theta}}, ^\circ$	$p$	$q$
$\eta_{\theta G1}$	184	2.3	0.93	0.92
$\eta_{\theta G2}$	182	1.8	2.00	1.98
$\eta_{\theta G3}$	181	1.3	2.00	2.00
$\eta_{\theta G4}$	178	3.2	2.00	2.00
$\eta_{\theta G5}$	176	5.4	2.00	2.00
$\eta_{\theta G6}$	175	4.9	1.87	2.00
$\eta_{\theta G7}$	172	10.2	2.00	2.00
$\eta_{\theta G8}$	174	7.9	2.00	1.98
$\eta_{\theta G9}$	173	11.0	1.91	1.89
$\eta_{\theta G10}$	174	10.1	2.00	1.98
$\eta_{\theta G11}$	172	8.3	1.81	2.00
$\eta_{\theta G12}$	173	10.1	2.00	1.98
Average	176	6.37	1.88	1.89

(a) Results for all wave gauges.



(b) Achieved order of convergence for all wave gauges.

Figure 17: Uncertainty analysis for wave elevation: second order phases.

Figure 18 presents the results for second order horizontal ( $x$  component) velocity amplitudes, where the average amplitude of 0.0342 m/s is obtained over all wave lengths, although with quite irregular results for different wave length. The numerical uncertainty ranges from 0.1% to very high 141.8%, which can be considered an outlier, increasing the average numerical uncertainty to 25.1%. Achieved orders of spatial and temporal accuracy range from 0.72 to 2.00, with averages values of 1.65 for both space and time.

Figure 19 presents the results for second order horizontal ( $x$  component) velocity phases, which shows quite irregular results for different wave gauges. The asymptotic solution ranges from  $130^\circ$  for the first wave probe to  $200^\circ$  for the last probe. On average, the guessed asymptotic solution is  $176^\circ$ , with the average uncertainty of  $13.1^\circ$ . The achieved order of spatial and temporal accuracy is 1.63 and 1.80, respectively, on average for all velocity probes.

Figure 20 presents the results for second order vertical ( $y$  component) velocity amplitudes. Similarly to second order horizontal velocity amplitudes, the asymptotic solutions are quite irregular for different wave probes, with the average value of 0.0324 m/s. The numerical uncertainty is 17.58% on average, where the largest uncertainty is obtained for velocity probe 5 with 76.2%, where a low order of temporal accuracy is achieved,  $q = 0.60$ . Averaged over all probes, achieved orders of spatial and temporal accuracy are 1.82 and 1.75, respectively.

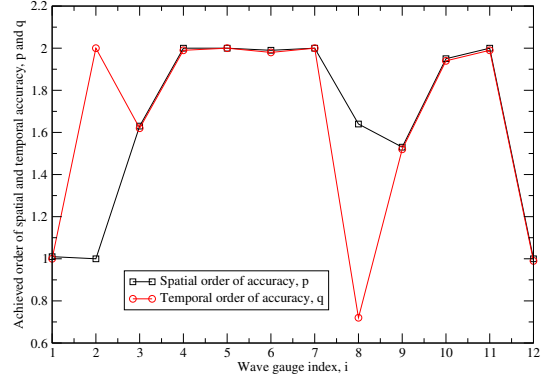
Figure 21 presents the results for second order vertical ( $y$  component) velocity phases. The guessed asymptotic solution for the phases varies from  $262^\circ$  to  $306^\circ$ , with the average value of  $274^\circ$ . The corresponding numerical uncertainty ranges from  $2.7^\circ$  to  $44.1^\circ$  obtained at velocity probe 10. The average numerical uncertainty is  $15.6^\circ$ , while the achieved orders of spatial and temporal accuracy are 1.66 and 1.54, respectively, averaged over all probes.



Item	$u_{xA}$ , m/s	$U_{U_{xA}}$ %	$p$	$q$
$u_{xAP1}$	$3.89 \times 10^{-2}$	8.5%	1.01	1.00
$u_{xAP2}$	$2.82 \times 10^{-2}$	27.0%	* 1.2	2.00
$u_{xAP3}$	$3.09 \times 10^{-2}$	17.7%	1.63	1.62
$u_{xAP4}$	$3.42 \times 10^{-2}$	0.1%	2.00	1.99
$u_{xAP5}$	$3.59 \times 10^{-2}$	17.8%	2.00	2.00
$u_{xAP6}$	$3.26 \times 10^{-2}$	6.5%	1.99	1.98
$u_{xAP7}$	$3.62 \times 10^{-2}$	18.1%	2.00	2.00
$u_{xAP8}$	$4.88 \times 10^{-2}$	141.8%	1.64	0.72
$u_{xAP9}$	$2.96 \times 10^{-2}$	17.9%	1.53	1.52
$u_{xAP10}$	$3.34 \times 10^{-2}$	6.5%	1.95	1.94
$u_{xAP11}$	$3.19 \times 10^{-2}$	9.7%	2.00	1.99
$u_{xAP12}$	$2.95 \times 10^{-2}$	29.5%	1.00	0.99
<b>Average</b>	$3.42 \times 10^{-2}$	25.09	1.65	1.65

\* 1,2 Fit was made using first and second order exponents

(a) Results for all probes.



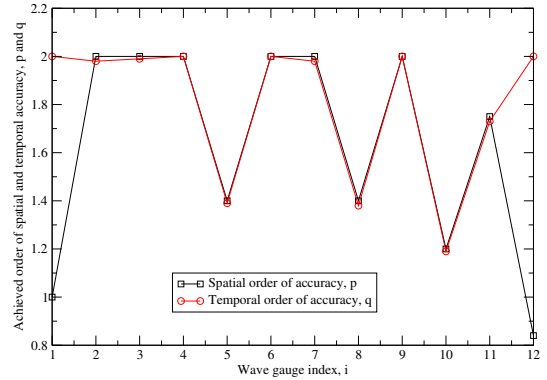
(b) Achieved order of convergence for all probes.

Figure 18: Uncertainty analysis for  $x$  (horizontal) component of the velocity field: second order amplitudes.

Item	$u_{x\theta}$ , °	$U_{U_{x\theta}}$ , °	$p$	$q$
$u_{x\theta P1}$	130	61.4	* 1.2	2.00
$u_{x\theta P2}$	175	26.8	2.00	1.98
$u_{x\theta P3}$	177	3.4	2.00	1.99
$u_{x\theta P4}$	179	2.9	2.00	2.00
$u_{x\theta P5}$	192	29.3	1.40	1.39
$u_{x\theta P6}$	166	12.8	2.00	2.00
$u_{x\theta P7}$	172	9.4	2.00	1.98
$u_{x\theta P8}$	171	16.7	1.40	1.38
$u_{x\theta P9}$	165	8.3	2.00	2.00
$u_{x\theta P10}$	197	45.4	1.20	1.19
$u_{x\theta P11}$	193	39.2	1.75	1.73
$u_{x\theta P12}$	200	26.6	0.84	2.00
<b>Average</b>	176	23.5	1.63	1.80

\* 1,2 Fit was made using first and second order exponents

(a) Results for all probes.



(b) Achieved order of convergence for all probes.

Figure 19: Uncertainty analysis for  $x$  (horizontal) component of the velocity field: second order phases.

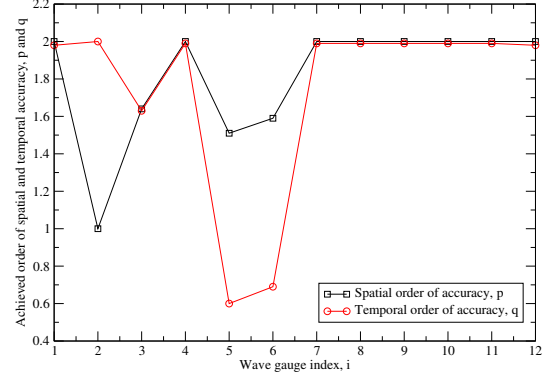
#### 4.1.2. Validation study for the progressive wave

The remainder of the analysis is dedicated to validation by comparing the results obtained with the present model with fully nonlinear, potential flow based stream function wave theory [59]. Figure 22 presents the comparison of first order wave elevations obtained with the fine grid (Grid 6) for all wave gauges ranging from  $x = 1\lambda$  to  $x = 12\lambda$ .

Item	$u_{yA}$ , m/s	$U_{U_{yA}}$ %	$p$	$q$
$u_{yAP1}$	$3.12 \times 10^{-2}$	9.2%	2.00	1.98
$u_{yAP2}$	$2.88 \times 10^{-2}$	17.5%	* 1,2	2.00
$u_{yAP3}$	$2.87 \times 10^{-2}$	15.4%	1.64	1.63
$u_{yAP4}$	$3.18 \times 10^{-2}$	0.4%	2.00	1.99
$u_{yAP5}$	$4.39 \times 10^{-2}$	76.2%	1.51	0.60
$u_{yAP6}$	$3.77 \times 10^{-2}$	52.9%	1.59	0.69
$u_{yAP7}$	$3.05 \times 10^{-2}$	4.5%	2.00	1.99
$u_{yAP8}$	$3.18 \times 10^{-2}$	1.0%	2.00	1.99
$u_{yAP9}$	$3.00 \times 10^{-2}$	19.3%	2.00	1.99
$u_{yAP10}$	$3.12 \times 10^{-2}$	4.5%	2.00	1.99
$u_{yAP11}$	$3.07 \times 10^{-2}$	6.1%	2.00	1.99
$u_{yAP12}$	$3.30 \times 10^{-2}$	3.9%	2.00	1.98
<b>Average</b>	$3.24 \times 10^{-2}$	17.58	1.82	1.75

\* 1,2 Fit was made using first and second order exponents

(a) Results for all probes.



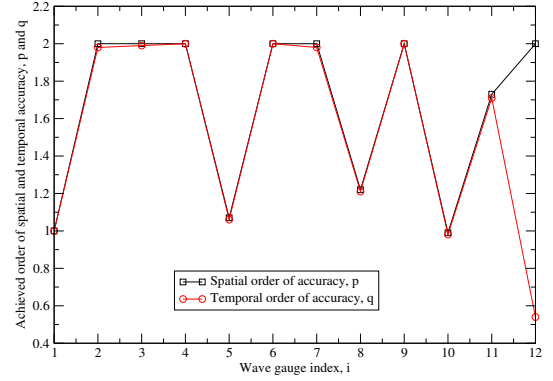
(b) Achieved order of convergence for all probes.

Figure 20: Uncertainty analysis for  $y$  (vertical) component of the velocity field: second order amplitudes.

Item	$u_{y\theta}$ , °	$U_{U_{y\theta}}$ , °	$p$	$q$
$u_{y\theta P1}$	262	7.0	* 1,2	1.00
$u_{y\theta P2}$	264	18.9	2.00	1.98
$u_{y\theta P3}$	267	2.7	2.00	1.99
$u_{y\theta P4}$	269	2.3	2.00	2.00
$u_{y\theta P5}$	298	32.4	1.07	1.06
$u_{y\theta P6}$	256	7.9	2.00	2.00
$u_{y\theta P7}$	263	5.9	2.00	1.98
$u_{y\theta P8}$	262	10.4	1.22	1.21
$u_{y\theta P9}$	257	5.0	2.00	2.00
$u_{y\theta P10}$	306	44.1	0.99	0.98
$u_{y\theta P11}$	283	24.1	1.73	1.71
$u_{y\theta P12}$	300	25.7	2.00	0.54
<b>Average</b>	274	15.6	1.66	1.54

\* 1,2 Fit was made using first and second order exponents

(a) Results for all probes.



(b) Achieved order of convergence for all probes.

Figure 21: Uncertainty analysis for  $y$  (horizontal) component of the velocity field: second order phases.

**Validation study for first order effects.** The dissipation error associated with Figure 22a increases downstream of the numerical wave tank and stabilises at approximately 3.81% at  $x = 8\lambda$ . The dissipation error is lowered at the last wave gauge since the relaxation zone starts to force the solution towards the target solution as discussed in Sec. 3. The dispersion error presented in Figure 22b shows similar trend, with the largest difference being slightly less than  $9^\circ$ .

Figure 23 presents the comparison of first order horizontal velocities obtained with the fine grid for all probes. Similarly to wave elevation, the dissipation causes the fluid to lose linear momentum downstream of the inlet. The error stabilises at approximately  $x = 7\lambda$  at 4.2% before it starts to tend to the stream function solution within the relax-

ation zone at  $x = 12\lambda$ . The phase difference presented in [Figure 23b](#) shows increasing trend downstream of the inlet, although with irregular and oscillatory behaviour. The largest dissipation error is found at  $x = 9\lambda$  with approximately  $10.3^\circ$ , which is comparable to  $9^\circ$  for wave elevation phase.

[Figure 24](#) presents the comparison of first order vertical velocities obtained with the fine grid for all probes. The trend for the vertical velocity is similar to the one obtained for the horizontal velocity. The dissipation error reaches a local maximum of approximately 3.3% at  $x = 8\lambda$ , suddenly growing to 5.7% within the start of the outlet relaxation zone at  $x = 12\lambda$ . This trend is different than the one observed for horizontal velocity component and wave elevation and needs to be investigated further. The dispersion of the vertical velocity field as presented in [Figure 24b](#) has exactly the same irregular trend as the dispersion of the horizontal velocity field. The maximum dispersion error is found at  $x = 9\lambda$  and the difference in phase is approximately  $10^\circ$  (compared to  $10.3^\circ$  for the horizontal velocity).

**Validation study for second order effects.** Compared to the first order wave elevation, the second order wave elevation exhibits a similar trend of increasing dissipation and dispersion errors downstream of the wave tank, as seen in [Figure 25](#). [Figure 25a](#) shows that the relative error of the second order wave amplitude increases up to approximately 7% at  $x = 8\lambda$ , while it is less than 1% until  $x = 4\lambda$ . The dispersion error grows continuously up to  $18^\circ$  at  $x = 9\lambda$ , where it stabilises. Similarly to first order effects, the solution starts to be gradually forced to the stream function solution in the last wave gauge at  $x = 12\lambda$  due to the relaxation zone.

[Figure 26a](#) shows the second order amplitude of the horizontal velocity component, where it is interesting to note that the solution obtained with the present model over-predicts the solution obtained with stream function wave theory. The maximum differences compared to stream function wave theory are obtained for probes that are within relaxation zones  $x = \lambda$  and  $x = 12\lambda$ . For probes not affected by relaxation zones ( $x = 2\lambda$  to  $x = 11\lambda$ ), the maximum difference is approximately 7%. The comparison of phases for the second order horizontal velocity is presented in [Figure 26b](#). As for the first order phases, the behaviour is quite irregular for different longitudinal locations, where the phase calculated with the present model lags behind from  $9^\circ$  at  $x = 2\lambda$  to  $32^\circ$  at  $x = 9\lambda$ .

The second order of vertical velocity presented in [Figure 27](#) shows similar behaviour as second order of horizontal velocity. The amplitude is over-predicted compared to stream function wave theory, as shown in [Figure 27a](#), where the maximum difference is approximately 10% obtained for probe at  $x = 12\lambda$ , while the minimum difference is 2% for probe at  $x = 6\lambda$ . The second order phases show irregular behaviour on different longitudinal locations, as shown in [Figure 27b](#). The difference ranges from less than  $2^\circ$  for probe  $x = 2\lambda$  to approximately  $18^\circ$  for  $x = 9\lambda$ .

**Field data comparison.** In addition to detailed data obtained with wave gauges and probes, we present a qualitative comparison of volume fraction and velocity fields in [Figure 28](#) for a part of the domain between  $x \approx 5.5\lambda$  and  $x \approx 7.5\lambda$

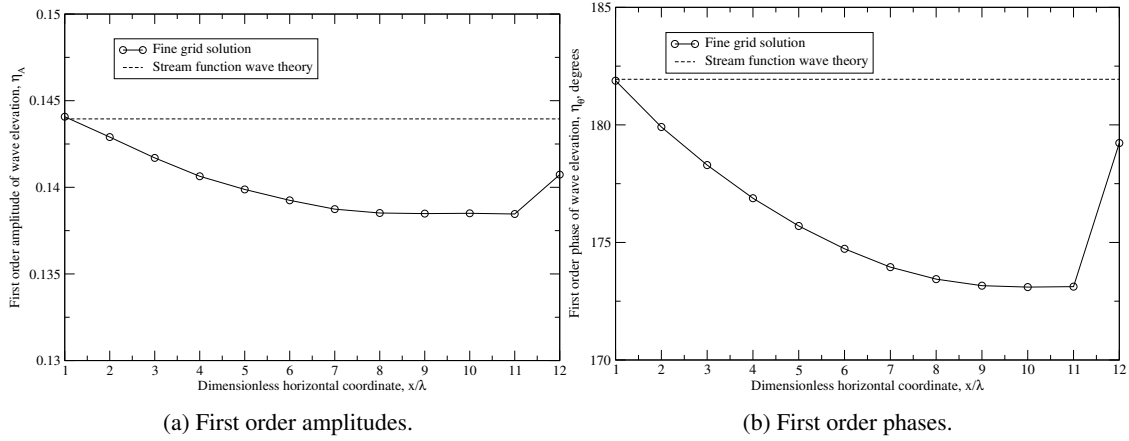


Figure 22: Comparison of fine grid (Grid 6) first order wave elevations with the stream function wave theory [59] for all wave gauges.

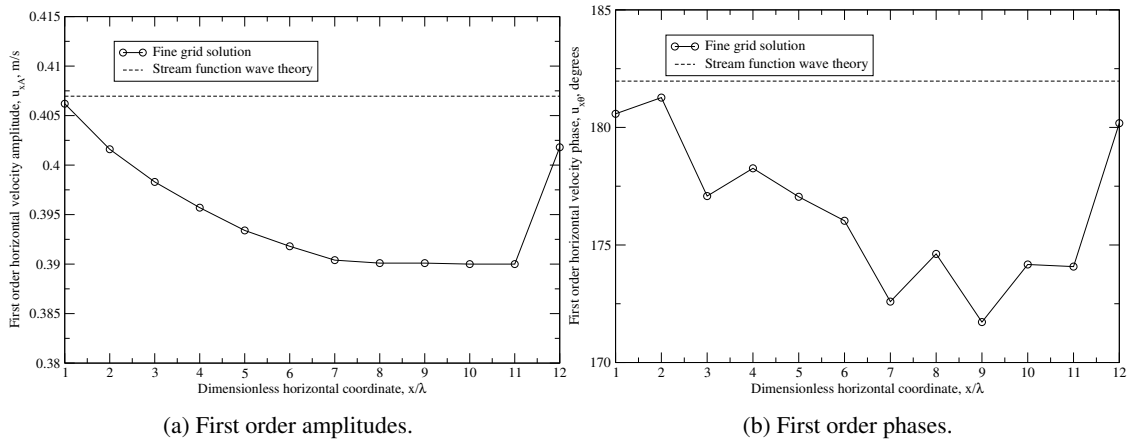


Figure 23: Comparison of fine grid (Grid 6) first order horizontal velocities with the stream function wave theory [59] for all probes.

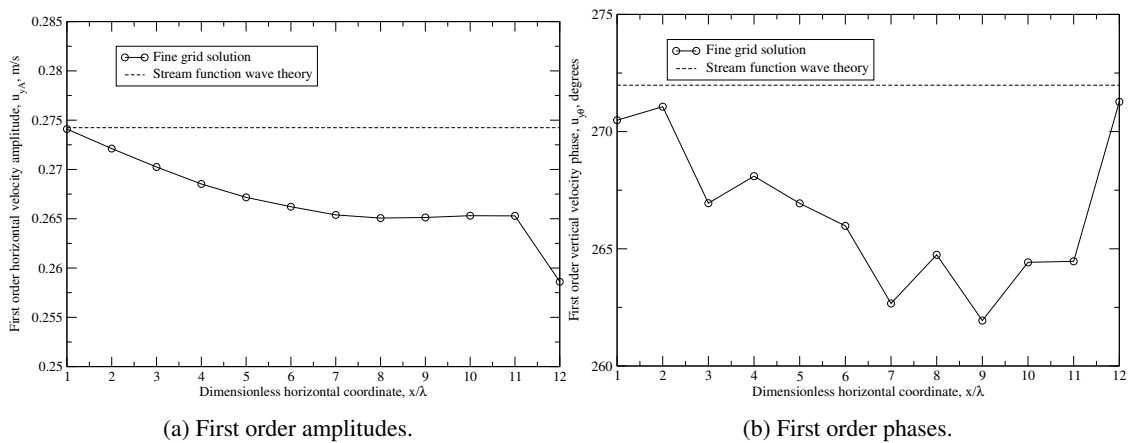


Figure 24: Comparison of fine grid (Grid 6) first order vertical velocities with the stream function wave theory [59] for all probes.

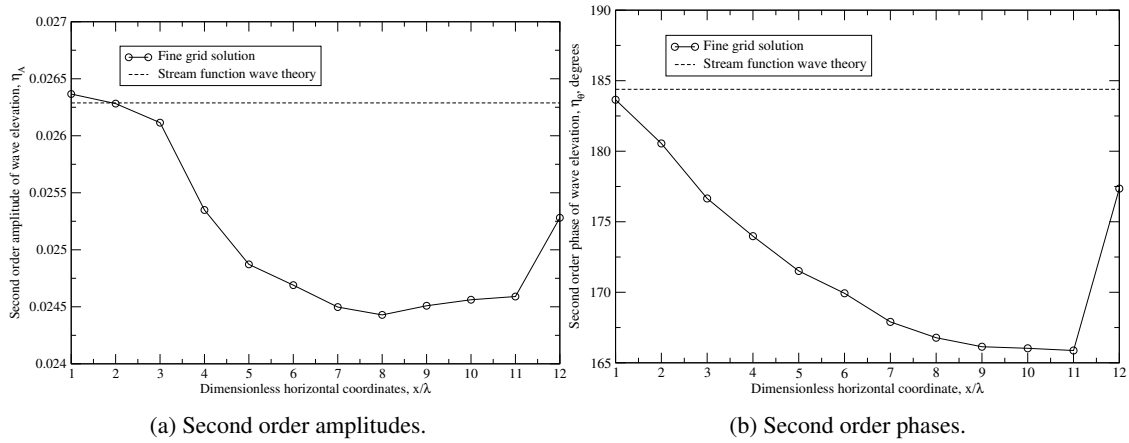


Figure 25: Comparison of fine grid (Grid 6) second order wave elevations with the stream function wave theory [59] for all wave gauges.

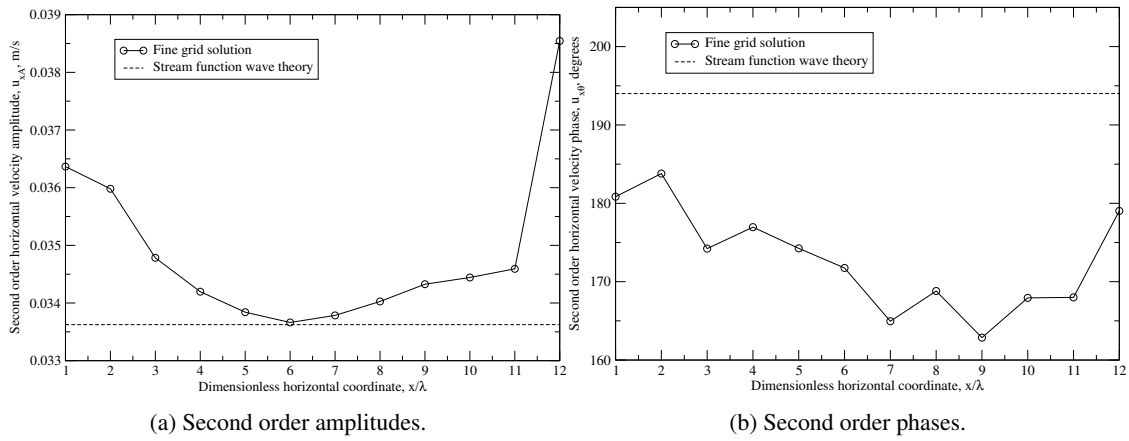


Figure 26: Comparison of fine grid (Grid 6) second order horizontal velocities with the stream function wave theory [59] for all probes.

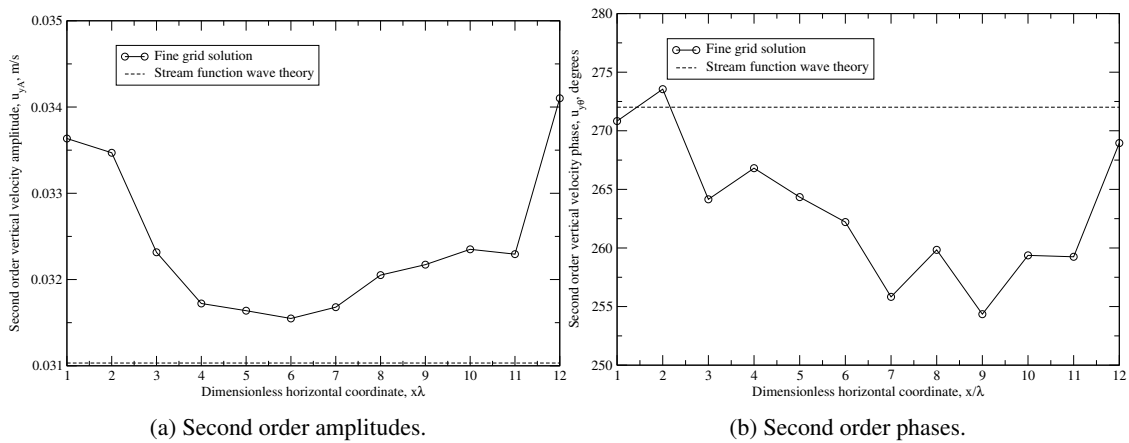


Figure 27: Comparison of fine grid (Grid 6) second order vertical velocities with the stream function wave theory [59] for all probes.

at  $t = 10T$  (end of simulation). Top figures present the solution obtained with the present model, while lower figures present the solution obtained using the stream function wave theory. Figure 28a shows that the free surface is well preserved without numerical diffusion of the volume fraction field  $\alpha$ . In the stream function solution, the velocity field is defined only up to the free surface, Figure 28b. The present model takes into account two-phase effects, thus producing an asymmetric velocity field above the free surface. The velocity field in the water compares well with the stream function wave theory.

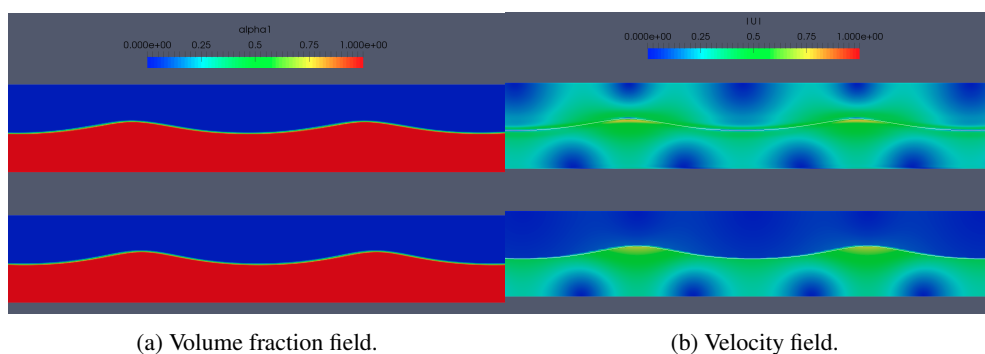


Figure 28: Volume fraction and velocity fields obtained with the present model (upper part) compared to stream function wave theory (lower part) in part of the domain between  $x \approx 5.5\lambda$  and  $x \approx 7.5\lambda$  at  $t = 10T$ .

**Note on two-phase effects and vorticity.** It is important to clearly state the differences between the two computational models compared within this study. Although the stream function wave theory accounts for nonlinearity in the potential flow context, it does not take into account two-phase, vorticity and viscosity effects. The present model takes into account all of these effects and can predict the velocity in the air phase as well, accounting for relevant jump conditions at the free surface. Figure 29 presents the velocity field obtained with the present model in the part of the domain between  $x \approx 6\lambda$  and  $x \approx 7\lambda$  at  $t = 10T$ , using the fine grid. The horizontal velocity component shown in Figure 29a changes sign across the free surface, *e.g.* below the wave crest, the horizontal velocity is positive (in the direction of wave propagation), while above the crest, it is negative (in the direction opposite of wave propagation). Along with the vertical velocity field presented in Figure 29b, this leads to significant vorticity effects near the free surface, as presented in Figure 29d. Note that the vorticity field defined as  $\omega = \nabla \times \mathbf{u}$  vanishes far from the free surface, where the potential flow model is therefore justified. Further investigation of the combined vorticity and viscosity effects on propagation of steep waves shall be the topic for future work.

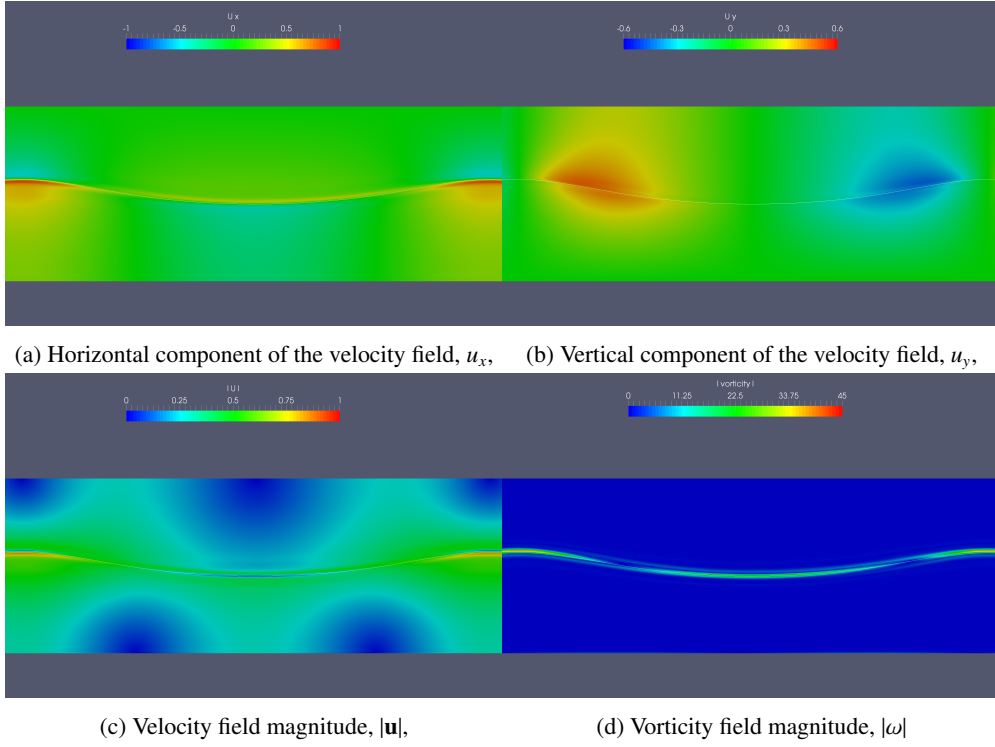


Figure 29: Velocity and vorticity fields in part of the domain between  $x \approx 6\lambda$  and  $x \approx 7\lambda$  at  $t = 10T$ .

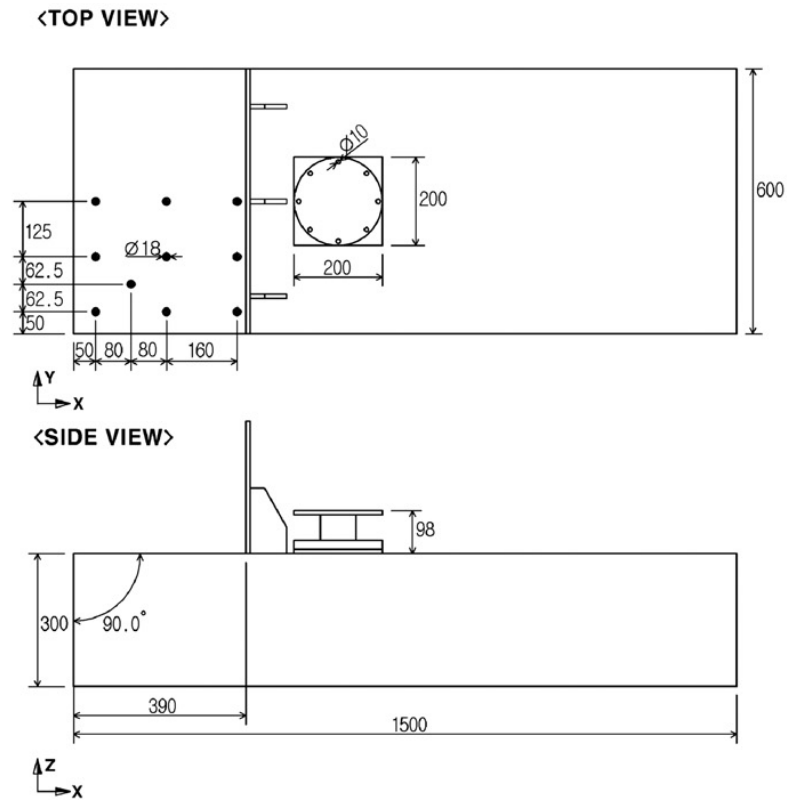
#### 4.2. Wave breaking on a simplified ship model

For the second test case, we investigate a violent free surface flow on a deck of a simplified ship-like structure in model scale. The structure presented in Figure 30 is taken from Lee *et al.* [48], who carried out comprehensive experimental analysis specifically for validation of various CFD codes. They performed comprehensive studies including three geometries, multiple regular waves impacting the structure and have measured pressure at ten locations on the deck in front of a breakwater, as depicted in Figure 30b. In this study, we consider a rectangular structure as presented in Figure 30a in a regular wave with parameters given in Table 3. The wave is moderately steep with  $kH/2 = 0.188$ , which is 7.5% steeper than the wave considered in Sec. 4.1.

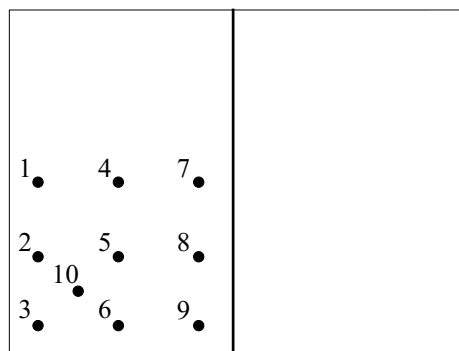
The computational domain is identical to Gatin *et al.* [63] and is presented in Figure 31. The relaxation zones are

Table 3: Wave parameters for the simplified ship model.

Wave height	$H$ , m	0.13
Wave length	$\lambda$ , m	2.25
Water depth	$d$ , m	1
Wave steepness	$kH/2$	0.188



(a) Dimensions of the model (in millimetres) and pressure gauge locations,



(b) Indexing of pressure gauges.

Figure 30: Geometry of the ship-like structure, courtesy of Lee *et al.* [48]

used at inlet, outlet, starboard and portside boundaries in order to prevent wave reflection and reduce the size of the computational domain. The domain is 6.5 metres long and the relaxation zones at inlet and outlet are 2.5 metres long. Height of the domain measured from the deck at which the pressure probes are positioned is 0.3 metres. Depth of the domain from the calm free surface to the bottom is 1 metre, while the width is 3 metres. Simulations have been



performed for 20 wave periods, while the time-step is controlled with a maximum Courant–Friedrichs–Lewy (CFL) number of 0.75.

The coarse computational grid is presented in [Figure 32](#), where [Figure 32a](#) shows the surface grid at the structure, and [Figure 32b](#) shows a slice through the longitudinal centre plane. The grid is structured with grading towards the deck in the vertical direction and towards the structure in the longitudinal direction. The coarse grid is designed with approximately 23 cells per wave amplitude and 225 cells per wave length near the structure, and consists of 276 699 cells. In order to assess numerical uncertainty, three additional grids are used with a constant refinement ratio of  $r = \sqrt{2}$  for all three spatial dimensions and time. Additional information regarding the grids is presented in [Table 4](#).

Table 4: Grids for the green–water case.

Grid index	1	2	3	4
Number of cells	276 699	518 476	1 077 515	2 181 103
Number of cells per wave length	225	318	450	637
Number of cells per wave height	23	33	46	65

#### 4.2.1. Verification study for the wave breaking case

Prior to comparing the CFD results with experimental data, we perform uncertainty assessment following the same guidelines by Eça and Hoekstra [47] as used for the wave propagation case. The focus is placed on pressure at ten pressure gauges positioned at the deck. The free surface flow at the deck exhibits complex flow patterns, [Figure 33](#). Therefore higher numerical uncertainties should be expected compared to wave propagation case. In addition, [Figure 34a](#) presents the pressure signal at pressure probe 3, indicating irregular behaviour in terms of pressure peaks. Due to irregularity of pressure peaks, the uncertainty assessment is carried using an average pressure impulse during last fifteen periods, defined as:

$$P = \frac{\sum_{i=0}^N \int_0^T p_i(\tau) d\tau}{N} \quad (37)$$

Average pressure impulses for all wave gauges are presented in [Figure 34b](#) for all grids. Convergence with grid refinement is not obtained for most of the pressure impulses. Nevertheless, the procedure presented by Eça and Hoekstra [47] yields reasonable estimates of numerical uncertainty even when monotonic convergence is not achieved. The verification results are summarized in [Figure 35](#), where the mean value of pressure impulse  $P$  for four grids is presented in the first column, while remaining columns represent numerical uncertainty, achieved order of spatial convergence and achieved order of temporal convergence, respectively. The numerical uncertainty ranges from 4.4% (pressure probe 5) to 38.4% (pressure probe 8), with the average value of 17.6%, which is significantly higher than the

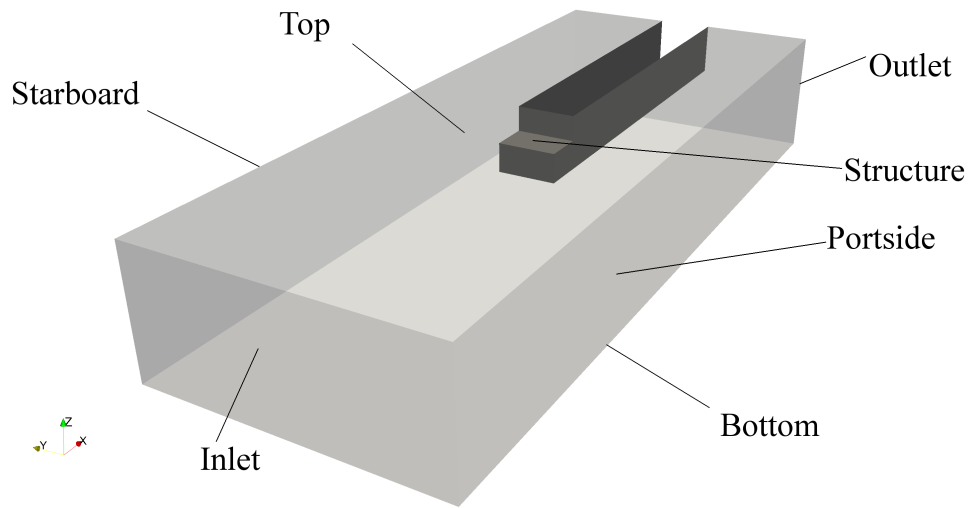


Figure 31: Perspective view of the computational domain.

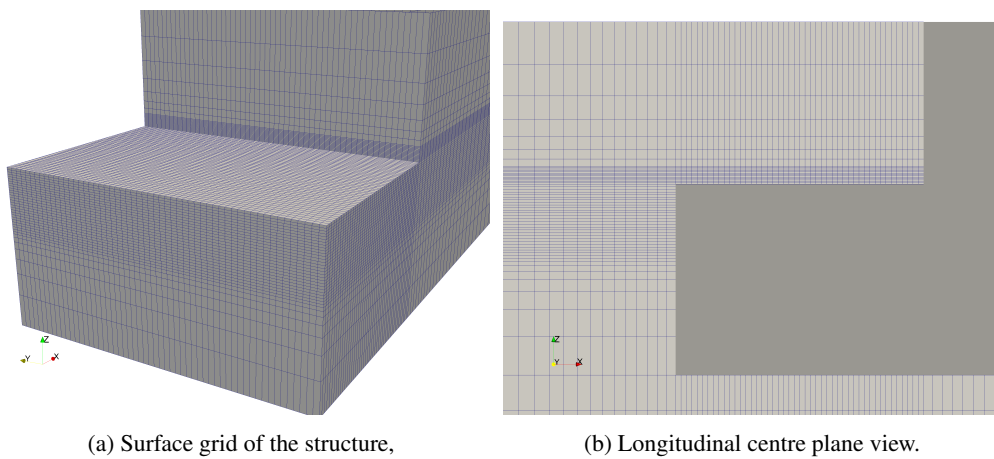


Figure 32: Coarse computational grid details.

numerical uncertainties for the wave propagation case. As most of the pressure impulses do not achieve convergence with grid refinement, the procedure by Eça and Hoekstra [47] estimates the order of convergence between first and second order. Such irregular behaviour is expected, considering the irregular behaviour of wave breaking during successive periods (see Figure 34a).

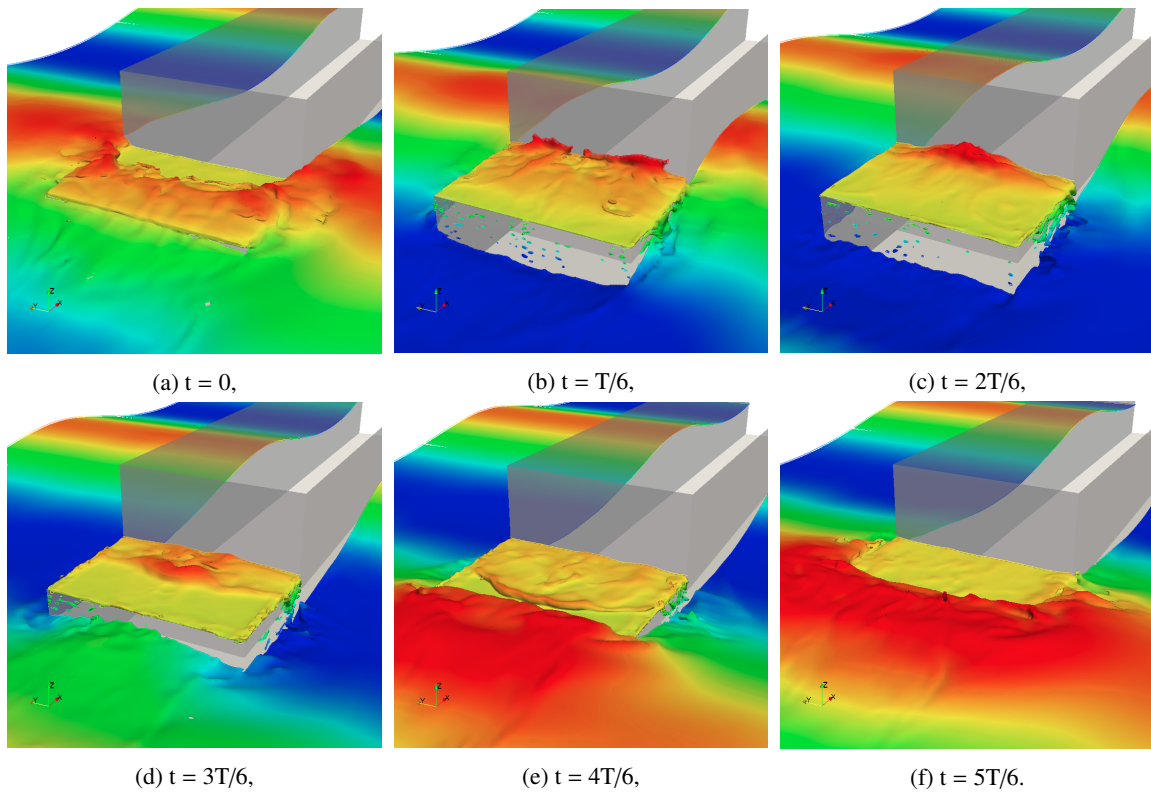
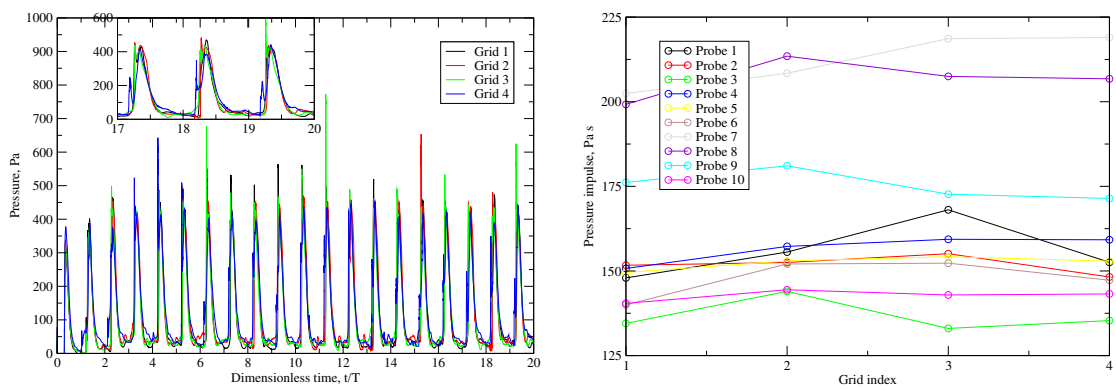


Figure 33: Perspective view of the computational results during the last period.



(a) Pressure signal at pressure probe 3 obtained with all grids. (b) Average pressure impulses with all four grids for all probes.

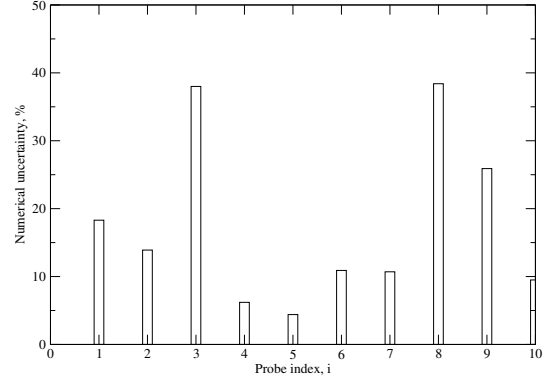
Figure 34: Grid refinement study results for pressure and pressure impulses.

Figure 35: Uncertainty analysis for pressure impulses for all pressure probes.

Item	$P$ , Pas	$U_p$ , %	$p$	$q$
$P_1$	156	18.3%	1.00	2.00
$P_2$	152	13.9%	1.39	0.59
$P_3$	137	38.0%	1.00	2.00
$P_4$	156	6.2%	* 1,2	2.00
$P_5$	152	4.4%	2.00	* 1,2
$P_6$	148	10.9%	2.00	2.00
$P_7$	212	10.7%	1.00	1.00
$P_8$	207	38.4%	* 1,2	2.00
$P_9$	175	25.9%	1.00	2.00
$P_{10}$	143	9.5%	2.00	* 1,2
Average	164	17.6	1.34	1.56

\* 1,2 Fit was made using first and second order exponents

(a) Results for all pressure probes.



(b) Numerical uncertainties.

#### 4.2.2. Validation study for the wave breaking case

Having assessed numerical uncertainties, the CFD results are compared with experimental measurements by Lee *et al.* [48]. Raw experimental data has been provided by Lee *et al.* [48], allowing us to perform identical post processing for period-averaged pressure impulses defined by Eqn. (37) for experimental and numerical data. The results are compared in Figure 36 for all wave gauges. The results obtained with the fine grid are used as reference computational results and are denoted with solid line and squares, while the experimental data is denoted with dashed line and circles. The results obtained with the present approach under-predict the experimental data for nine out of ten pressure probes. The minimum relative error compared to experiments is approximately +4% for probe 5, while the maximum error is approximately -26% for probe 1. On average, the relative error between present results and experiments is -14%, while the estimated numerical uncertainty is approximately 18% on average (see Figure 35). The reader is referred to Lee *et al.* [48] for detailed analysis and discussion on experimental uncertainty, which is of the same order as the numerical uncertainty.

## 5. Conclusion and future work

This paper presented a numerical model with sharp free surface treatment within the Finite Volume framework. The model is based on a combination of the Ghost Fluid Method for free surface jump conditions and the `isoAdvector` geometric scheme for reconstruction and advection of the volume fraction field. Although the method has been derived and implemented following the arbitrary polyhedral Finite Volume approach in the open source software OpenFOAM, all considered test cases have used structured hexahedral grids in order to more reliably estimate the achieved orders

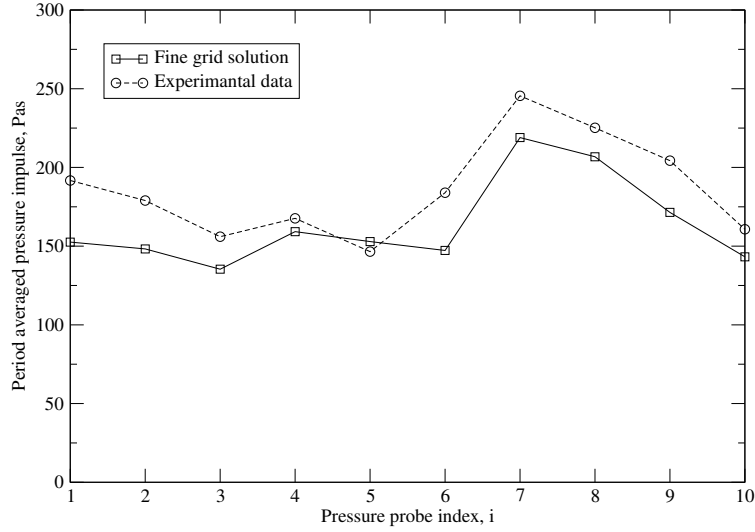


Figure 36: Comparison of pressure impulses with experimental data.

of accuracy.

Two test cases have been considered: moderately steep ( $kH/2 = 0.174$ ) wave propagation and wave breaking case on a simplified ship model. The wave propagation case was simulated with six grids with uniform refinement ratio in space and time, allowing us to estimate numerical uncertainty following the latest guidelines by Eça and Hoekstra [47]. Although the implemented method is formally second order accurate, the observed order of accuracy is between first and second order based on 144 measured items (12 wave gauges and velocity probes  $\times$  3 signals (elevation, horizontal and vertical velocity)  $\times$  4 items (first and second order amplitudes and phases)). Averaged over all items, the achieved orders of spatial and temporal accuracy are 1.59 and 1.60, respectively. The first order amplitudes of wave elevation and velocity have numerical uncertainty which is 3.1% on average, while second order effects have higher numerical uncertainty of 18.3% on average, which is expected since the second order effects are an order of magnitude smaller than the first order effects. Similarly, the average numerical uncertainty for first order phases is  $8.2^\circ$ , while it is  $15.2^\circ$  for second order phases. Since the achieved order of accuracy is between first and second order, we expect to have certain amount of dissipation errors with the present model. Considering a domain that is 13 wave lengths long allowed us to quantify dissipation and dispersion errors along the numerical wave tank. The smallest differences (often within 2% for all items) are obtained within the first four wave lengths down the numerical wave tank. The differences tend to grow until  $x = 8\lambda$  where they stabilise. The maximum error for first order amplitudes of wave elevation and velocity is 3.8% on average, while the second order amplitudes show a discrepancy of approximately 8%. The maximum dissipation error for first order effects is approximately  $9.8^\circ$  on average for wave elevation and two velocity components, while it is larger for second order effects:  $22.7^\circ$ .

This extensive study revealed that the dissipation and dispersion errors stabilise at  $x \in [7\lambda, 9\lambda]$ , while the errors are smaller closer to the incoming boundary ( $x = 0$ ). Therefore, smaller errors will be obtained if one considers a domain with only *e.g.* five wave lengths.

The wave breaking case on a simplified ship model simulated with four systematically refined grids revealed that the numerical uncertainties for pressure impulses measured at the deck are significantly higher: ranging from approximately 5 to 40%. There are two reasons for higher numerical uncertainties that are associated with irregular behaviour of pressure peaks during successive wave periods, which shall be investigated in future:

- The inability of the present model to take into account the air compressibility. It is possible that the compressibility of air is important for such a violent free surface flow, which should in turn smooth out the pressure peaks upon impact.
- Under-resolved physical scales. It is also possible that for such a violent flow, the nonlinearity of governing equations causes significant non-periodic behaviour even with periodic boundary conditions. Note that the finest grid considered had approximately two million cells, which is orders of magnitude smaller than scale-resolving simulations [2].

The averaged pressure impulses measured at ten wave gauges showed good comparison with experimental data.

With these two test cases, the model has been extensively verified and validated regarding wave propagation problems, although certain observations need to be investigated in future:

- Achieved orders of accuracy generally show irregular behaviour for different horizontal locations of wave gauges and probes. It is possible that the interplay of dissipation and dispersion errors needs to be addressed in a better way.
- The dispersion error for velocity shows slight oscillatory behaviour for different horizontal locations, while this is not observed for wave elevation.
- Quantifying the two-phase, vorticity and viscosity effects for wave propagation might reveal additional insights into dissipation mechanisms for steep waves.

## Acknowledgements

The authors are grateful to Prof. Luís Eça, Dr. Martin Hoekstra and Dr. Guilherme Vaz for sharing their numerical uncertainty analysis toolbox with the public [61]. The toolbox has been extensively used in this study due to immense quantity of data, saving us quite a lot of time and effort and enabling us to adhere to recent verification and validation guidelines.

## References

- [1] X. Yu, K. Hendrickson, D. K.-P. Yue, Air Entrainment in Free Surface Turbulence, in: Proceedings of the 31st Symposium on Naval Hydrodynamics, 2016.
- [2] L. Deike, W. Melville, S. Popinet, Air entrainment and bubble statistics in breaking waves, *J. Fluid Mech.* 801 (2016) 91–129.
- [3] L. Larsson, F. Stern, M. Visonneau, Numerical Ship Hydrodynamics: An assessment of the Gothenburg 2010 workshop, Springer, 2013. doi:10.1007/978-94-007-7189-5.
- [4] F. Stern, J. Yang, Z. Wang, H. Sadat-Hosseini, M. Mousaviraad, B. S., T. Xing, Computational Ship Hydrodynamics: Nowadays and Way Forward, in: Proceedings of the 29<sup>th</sup> ONR Symposium on Naval Hydrodynamics, 2012, pp. 1–73.
- [5] P. Higuera, I. Losada, J. L. Lara, Three-dimensional numerical wave generation with moving boundaries, *Coast. Eng.* 101 (2015) 35–47.
- [6] B. T. Paulsen, H. Bredmose, H. B. Bingham, N. G. Jacobsen, Forcing of a bottom-mounted circular cylinder by steep regular water waves at finite depth, *J. Fluid Mech.* 755 (2014) 1–3. doi:10.1017/jfm.2014.386.
- [7] V. Vukčević, H. Jasak, I. Gatin, S. Malenica, Seakeeping Sensitivity Studies Using the Decomposition CFD Model Based on the Ghost Fluid Method, in: Proceedings of the 31st Symposium on Naval Hydrodynamics, 2016.
- [8] V. Vukčević, H. Jasak, Validation and Verification of Decomposition Model Based on Embedded Free Surface Method for Oblique Wave Seakeeping Simulations, in: Proceedings of the Tokyo 2015: A Workshop on CFD in Ship Hydrodynamics, Vol. 3, 2015.
- [9] F. R. Batchelor, An Introduction to Fluid Dynamics, Cambridge University Press, 1967.
- [10] C. Dopazo, On conditional averages for intermittent turbulent flows, *J. Fluid Mech.* 81 (1977) 433–438.
- [11] O. Ubbink, R. I. Issa, A method for capturing sharp fluid interfaces on arbitrary meshes, *J. Comput. Phys.* 153 (1999) 26–50.
- [12] N. G. Jacobsen, D. R. Fuhrman, J. Fredsøe, A wave generation toolbox for the open-source CFD library: OpenFoam®, *Int. J. Numer. Meth. Fluids* 70 (9) (2012) 1073–1088. doi:10.1002/flid.2726.
- [13] P. Higuera, J. Lara, I. J. Losada, Realistic wave generation and active wave absorption for Navier-Stokes models: Application to OpenFoam®, *Coast. Eng.* 71 (2013) 102–118. doi:10.1016/j.coastaleng.2012.07.002.
- [14] B. T. Paulsen, H. Bredmose, H. B. Bingham, An efficient domain decomposition strategy for wave loads on surface piercing circular cylinders, *Coast. Eng.* 86 (2014) 57–76. doi:10.1016/j.coastaleng.2014.01.006.
- [15] G. Lupieri, T. Puzzer, G. Contento, Numerical study of the wave-wave interaction by viscous flow simulations with OpenFOAM, in: XXI Symposium Sorta, 2014.
- [16] R. P. Fedkiw, T. Aslam, B. Merriman, S. Osher, A non-oscillatory eulerian approach to interfaces in multimaterial flows (the ghost fluid method), *J. Comput. Phys.* 152 (1999) 457–492.
- [17] R. P. Fedkiw, T. Aslam, S. Xu, The ghost fluid method for deflagration and detonation discontinuities, *J. Comput. Phys.* 154 (2) (1999) 393–427.
- [18] S. Wang, J. Glimm, R. Samulyak, X. Jiao, C. Diao, An Embedded Boundary Method for Two Phase Incompressible Flow, ArXiv e-prints. arXiv:1304.5514.
- [19] E. Olsson, G. Kreiss, A conservative level set method for two phase flow, *J. Comput. Phys.* 210 (1) (2005) 225–246.
- [20] O. Desjardins, V. Moureau, H. Pitsch, An accurate conservative level set/ghost fluid method for simulating turbulent atomization, *J. Comput. Phys.* 227 (18) (2008) 8395–8416.
- [21] W. Bo, J. W. Grove, A volume of fluid method based ghost fluid method for compressible multi-fluid flows, *Comput. Fluids* 90 (2014) 113–122.
- [22] B. Lalanne, L. R. Villegas, S. Tanguy, F. Risso, On the computation of viscous terms for incompressible two-phase flows with level set/ghost fluid method, *J. Comput. Phys.* 301 (2015) 289–307.

- [23] P. Queutey, M. Visonneau, An interface capturing method for free-surface hydrodynamic flows, *Comput. Fluids* 36 (2007) 1481–1510. doi:10.1002/j.compfluid.2006.11.007.
- [24] J. Huang, P. M. Carrica, F. Stern, Coupled ghost fluid/two-phase level set method for curvilinear body-fitted grids, *Int. J. Numer. Meth. Fluids* 44 (2007) 867–897. doi:10.1002/flid.1499.
- [25] V. Vukčević, H. Jasak, I. Gatin, Implementation of the Ghost Fluid Method for Free Surface Flows in Polyhedral Finite Volume Framework, *Comput. Fluids* 153 (2017) 1–19. doi:10.1016/j.compfluid.2017.05.003.
- [26] H. Rusche, Computational fluid dynamics of dispersed two - phase flows at high phase fractions, Ph.D. thesis, Imperial College of Science, Technology & Medicine, London (2002).
- [27] G. Tryggvason, R. Scardovelli, S. Zaleski, *Direct Numerical Simulations of Gas-Liquid Multiphase Flows*, Cambridge University Press, 2011.
- [28] E. Aulisa, S. Manservigi, R. Scardovelli, S. Zaleski, A geometrical area-preserving Volume-of-Fluid advection method, *J. Comput. Phys* 192 (1). doi:10.1016/j.jcp.2003.07.003.
- [29] J. Roenby, H. Bredmose, H. Jasak, A computational method for sharp interface advection, *Royal Society Open Science* 3 (11). doi:10.1098/rsos.160405.
- [30] J. A. Sethian, *Level Set Methods: Evolving Interfaces in Geometry, Fluid Mechanics, Computer Vision and Materials Science*, Cambridge University Press, 1996.
- [31] S. Osher, R. Fedkiw, *Level Set Methods and Dynamic Implicit Surfaces*, Springer, 2003.
- [32] E. Olsson, G. Kreiss, S. Zahedi, A conservative level set method for two phase flow ii, *J. Comput. Phys.* 225 (1) (2007) 785–807.
- [33] P. Gómez, J. Hernández, J. López, On the reinitialization procedure in a narrow-band locally refined level set method for interfacial flows, *Int. J. Numer. Methods Eng.* 63 (2005) 1478–1512.
- [34] D. Hartmann, M. Meinke, W. Schröder, Differential equation based constrained reinitialization for level set methods, *J. Comput. Phys.* 227 (2008) 6821–6845.
- [35] Y. Sun, C. Beckermann, Sharp interface tracking using the phase-field equation, *J. Comput. Phys.* 220 (2007) 626–653. doi:10.1016/j.jcp.2007.05.025.
- [36] Y. Sun, C. Beckermann, A two-phase diffusive-interface model for Hele-Shaw flows with large property contrasts, *Physica D* 237 (2008) 3089–3098. doi:10.1016/j.physd.2008.06.010.
- [37] V. Vukčević, H. Jasak, S. Malenica, Decomposition model for naval hydrodynamic applications, Part I: Computational method, *Ocean Eng.* 121 (2016) 37–46. doi:10.1016/j.oceaneng.2016.05.022.
- [38] V. Vukčević, H. Jasak, S. Malenica, Decomposition model for naval hydrodynamic applications, Part II: Verification and validation, *Ocean Eng.* 121 (2016) 76–88. doi:10.1016/j.oceaneng.2016.05.021.
- [39] J. López, C. Zanzi, P. Gómez, F. Faura, J. Hernández, A new volume of fluid method in three dimensions - Part II: Piecewise-planar interface reconstruction with cubic-Bézier fit, *International Journal for Numerical Methods in Fluids* 58 (8) (2008) 923–944. arXiv:fld.1, doi:10.1002/flid.1775.
- [40] J. Hernández, J. López, P. Gómez, C. Zanzi, F. Faura, A new volume of fluid method in three dimensions - Part I: Multidimensional advection method with face-matched flux polyhedra, *International Journal for Numerical Methods in Fluids* 58 (8) (2008) 897–921. arXiv:fld.1, doi:10.1002/flid.1776.
- [41] H. T. Ahn, M. Shashkov, Multi-material interface reconstruction on generalized polyhedral meshes, *Journal of Computational Physics* 226 (2) (2007) 2096–2132. doi:10.1016/j.jcp.2007.06.033.
- [42] B. Xie, S. Li, F. Xiao, An efficient and accurate algebraic interface capturing method for unstructured grids in 2 and 3 dimensions: The



- THINC method with quadratic surface representation, *International Journal for Numerical Methods in Fluids* 76 (12) (2014) 1025–1042. [arXiv:f1d.3968](https://arxiv.org/abs/1405.0829), [doi:10.1002/flid.3968](https://doi.org/10.1002/flid.3968).
- [43] J. Roenby, B. E. Larsen, H. Bredmose, H. Jasak, A New Volume-of-Fluid Method in Openfoam, in: VII International Conference on Computational Methods in Marine Engineering, MARINE 2017, 2017, pp. 1–12.
- [44] P. Higuera, J. Lara, I. J. Losada, Simulating coastal engineering processes with OpenFoam®, *Coast. Eng.* 71 (2013) 119–134. [doi:10.1016/j.coastaleng.2012.06.002](https://doi.org/10.1016/j.coastaleng.2012.06.002).
- [45] P. Roache, Quantification of uncertainty in computational fluid dynamics, *Ann. Rev. Fluid. Mech.* 29 (1997) 123–160.
- [46] F. Stern, R. V. Wilson, H. W. Coleman, E. G. Paterson, Comprehensive Approach to Verification and Validation of CFD Simulations—Part 1: Methodology and Procedures, *J. Fluids. Eng* 123(4) (2001) 793–802. [doi:10.1115/1.1412235](https://doi.org/10.1115/1.1412235).
- [47] Eça, L. and Hoekstra, M., A procedure for the estimation of the numerical uncertainty of cfd calculations based on grid refinement studies, *J. Comput. Phys.* 262 (2014) 104–130. [doi:10.1016/j.jcp.2014.01.006](https://doi.org/10.1016/j.jcp.2014.01.006).
- [48] H.-H. Lee, H.-J. Lim, S. H. Rhee, Experimental investigation of green water on deck for a CFD validation database, *Ocean Engineering* 42 (2012) 47–60. [doi:10.1016/j.oceaneng.2011.12.026](https://doi.org/10.1016/j.oceaneng.2011.12.026).
- [49] V. Vukčević, Numerical modelling of coupled potential and viscous flow for marine applications - in preparation, Ph.D. thesis, Faculty of Mechanical Engineering and Naval Architecture, University of Zagreb, PhD Thesis (2016). [doi:10.13140/RG.2.2.23080.57605](https://doi.org/10.13140/RG.2.2.23080.57605).
- [50] H. Jasak, Error analysis and estimation for the finite volume method with applications to fluid flows, Ph.D. thesis, Imperial College of Science, Technology & Medicine, London (1996).
- [51] S. V. Patankar, D. B. Spalding, A calculation procedure for heat, mass and momentum transfer in three-dimensional parabolic flows, *Int. J. Heat Mass Transf.* 15 (1972) 1787–1806.
- [52] R. I. Issa, Solution of the implicitly discretised fluid flow equations by operator-splitting, *J. Comput. Phys.* 62 (1986) 40–65.
- [53] C. M. Rhie, W. L. Chow, A numerical study of the turbulent flow past an isolated airfoil with trailing edge separation, *AIAA J.* 21 (1983) 1525–1532.
- [54] Z. Tuković, H. Jasak, A moving mesh finite volume interface tracking method for surface tension dominated interfacial fluid flow, *Comput. Fluids* 55 (2012) 70–84.
- [55] I. Demirdžić, On the Discretization of the Diffusion Term in Finite-Volume Continuum Mechanics, *Numer. Heat Transfer, Part B* 68 (2015) 1–10. [doi:10.1080/10407790.2014.985992](https://doi.org/10.1080/10407790.2014.985992).
- [56] J. H. Ferziger, M. Peric, *Computational Methods for Fluid Dynamics*, Springer, 1996.
- [57] H. Jasak, V. Vukčević, I. Gatin, Numerical Simulation of Wave Loads on Static Offshore Structures, in: *CFD for Wind and Tidal Offshore Turbines*, Springer Tracts in Mechanical Engineering, 2015, pp. 95–105.
- [58] F. Denner, B. G. Van Wachem, Fully-coupled balanced-force VOF framework for arbitrary meshes with least-squares curvature evaluation from volume fractions, *Numerical Heat Transfer, Part B: Fundamentals* 65 (3) (2014) 218–255. [arXiv:1405.0829](https://arxiv.org/abs/1405.0829), [doi:10.1080/10407790.2013.849996](https://doi.org/10.1080/10407790.2013.849996).
- [59] M. M. Rienecker, J. D. Fenton, A Fourier approximation method for steady water waves, *J. Fluid Mech.* 104 (1981) 119–137.
- [60] R. G. Dean, R. A. Dalrymple, *Water Wave Mechanics for Engineers and Scientists*, Vol. 2: Advanced Series on Ocean Engineering, World Scientific, 2010.
- [61] ReFRESH V&V Tools, <http://www.refresco.org/verification-validation/utilitiesvv-tools/>, [Online; accessed 10 October 2017] (2017).
- [62] Eça, L. and Vaz, G. and Hoekstra, M., Iterative Errors in Unsteady Flow Simulations: Are they Really Negligible?, in: *Proceedings of the 20th Numerical Towing Tank Symposium (NUTTS2017)*, 2017.

[63] Gatin, I. and Vukčević, V. and Jasak, H. and Seo, J. and Rhee, S.-H., CFD Verification and Validation of Green Sea Loads, Ocean Eng. Accepted for publication.